Curry, W.B., Shackleton, N.J., Richter, C., et al., 1995
Proceedings of the Ocean Drilling Program, Initial Reports, Vol. 154

2. EXPLANATORY NOTES[1]

Shipboard Scientific Party[2]

INTRODUCTION

In this chapter, we have assembled information that will help the reader understand the basis for our preliminary conclusions and also help the interested investigator select samples for further analysis. This information concerns only shipboard operations and analyses described in the site reports in the *Initial Reports* volume of the Leg 154 *Proceedings of the Ocean Drilling Program.* Methods used by various investigators for shore-based analyses of Leg 154 data will be detailed in the individual scientific contributions published in the *Scientific Results* volume.

Authorship of Site Chapters

The separate sections of the site chapters were written by the following shipboard scientists (authors are listed in alphabetical order, with no seniority implied):

Site Summary: Curry, Shackleton
Background and Scientific Objectives: Curry, Shackleton
Operations: Foss, Richter
Lithostratigraphy: Bickert, Cullen, Dobson, Harris, Maruyama, Tiedemann, Weedon, Zachos
Biostratigraphy: Backman, Chaisson, Pearson, Raffi, Yasuda
Paleomagnetism: Schneider, Valet
Composite Sections: Hagelberg
Sediment Accumulation Rates: Backman
Inorganic Geochemistry: Hampt, Murray
Physical Properties: Grützner, Herbert, Moran
Downhole Measurements: Bassinot, Ewart, deMenocal,
Summary and Conclusions: Curry, Shackleton

Following the text of each site chapter are summary core descriptions ("barrel sheets") and photographs of each core.

Use of "Ma" vs. "m.y."

1. *Ma* is equivalent to and replaces m.y. B.P. (million years Before Present); for example, 35–40 Ma.
2. *m.y.* is used in sentences such as ". . . for 5 m.y. in the early Miocene."

Drilling Characteristics

Information concerning sedimentary characteristics in uncored or unrecovered intervals may be inferred from seismic data and wireline-logging results, and from an examination of the behavior of the drill string, as observed and recorded on the drilling platform. Typically, the harder a layer, the slower and more difficult it is to penetrate. A number of other factors may determine the rate of penetration, so it is not always possible to relate the drilling time directly to the hardness of the layers. Bit weight and revolutions per minute, recorded on the drilling recorder, also influence the penetration rate.

[1] Curry, W.B., Shackleton, N.J., Richter, C., et al., 1995. *Proc. ODP, Init. Repts.,* 154: College Station, TX (Ocean Drilling Program).
[2] The Shipboard Scientific Party is as given in the list of participants preceding the Table of Contents.

Drilling Deformation

When cores are split, many show signs of significant sediment disturbance, including the concave-downward appearance of originally horizontal bands, the haphazard mixing of lumps of different lithologies (mainly at the tops of cores), and the near-fluid state of some sediments recovered from tens to hundreds of meters below the seafloor. Most core deformation probably occurs during cutting, but retrieval (with accompanying changes in pressure and temperature) and core handling on deck may also contribute.

Shipboard Scientific Procedures

Numbering of Sites, Holes, Cores, and Samples

ODP drill sites are numbered consecutively and refer to one or more holes drilled while the ship was positioned over one acoustic beacon. Multiple holes may be drilled at a single site by pulling the drill pipe above the seafloor (out of the hole), moving the ship some distance from the previous hole, and then drilling another hole.

For all ODP drill sites, a letter suffix designates each hole drilled at the site. The first hole drilled is assigned the site number modified by the suffix "A," the second hole takes the site number and suffix "B," and so forth. Note that this procedure differs slightly from that used by DSDP (Sites 1 through 624), but it prevents ambiguity between site- and hole-number designations. It is important to distinguish among holes drilled at a site because recovered sediments or rocks from different holes usually do not come from exactly equivalent positions in the stratigraphic column.

The cored interval is measured in meters below seafloor (mbsf). The depth interval assigned to an individual core begins with the depth below the seafloor that the coring operations began and extends to the depth that the coring operations ended (see Fig. 1). Each cored interval is generally 9.5 m long, which is the length of a core barrel. Coring intervals may be shorter and may not necessarily be adjacent if separated by drilled intervals. In soft sediments, the drill string can be "washed ahead" with the core barrel in place without recovering sediments. This is achieved by pumping water down the pipe at high pressure to wash the sediment out of the way of the bit and up the space between the drill pipe and the wall of the hole. If thin, hard, rock layers are present, then it is possible to get "spotty" sampling of these resistant layers within the washed interval and thus to have a cored interval greater than 9.5 m. When drilling hard rock, a center bit may replace the core barrel if it is necessary to drill without core recovery.

Cores taken from a hole are numbered serially from the top of the hole downward. Core numbers and their associated cored intervals (in meters below seafloor) ideally are unique in a given hole; however, this may not be true if an interval is cored twice, if the borehole wall caves in, or if other hole problems occur. Full recovery for a single core is 9.5 m of rock or sediment contained in a plastic liner (6.6 cm internal diameter) plus about 0.2 m (without a plastic liner) in the core catcher (Fig. 2). The core catcher is a device at the bottom of the core barrel that prevents the core from sliding out when the barrel is being retrieved from the hole. In many APC/XCB cores, recovery exceeds the 9.5-m theoretical maximum by as much as 0.60 m. The cause of this expansion is not fully understood. The recovered core in its liner is divided into 1.5-m sections that are numbered serially from the top

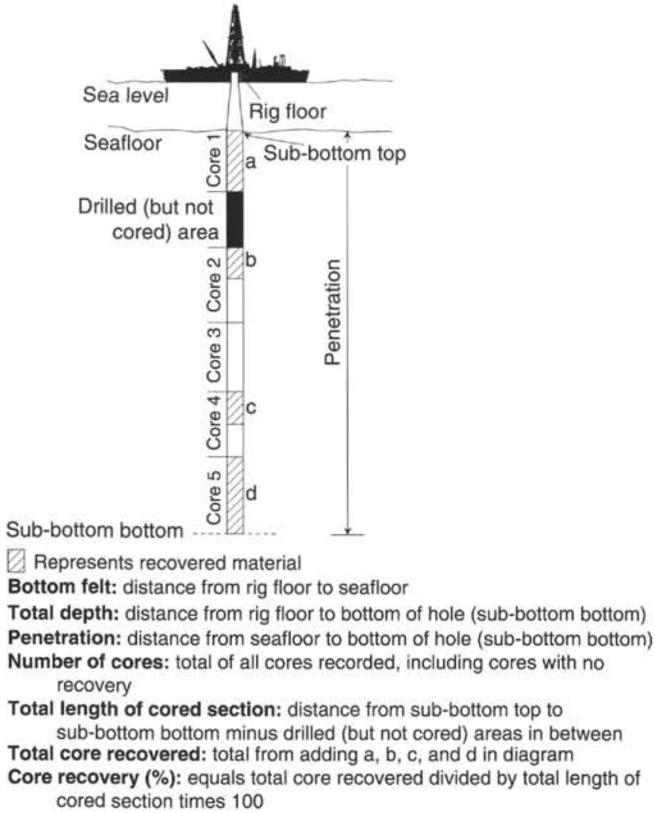

Figure 1. Coring and depth intervals.

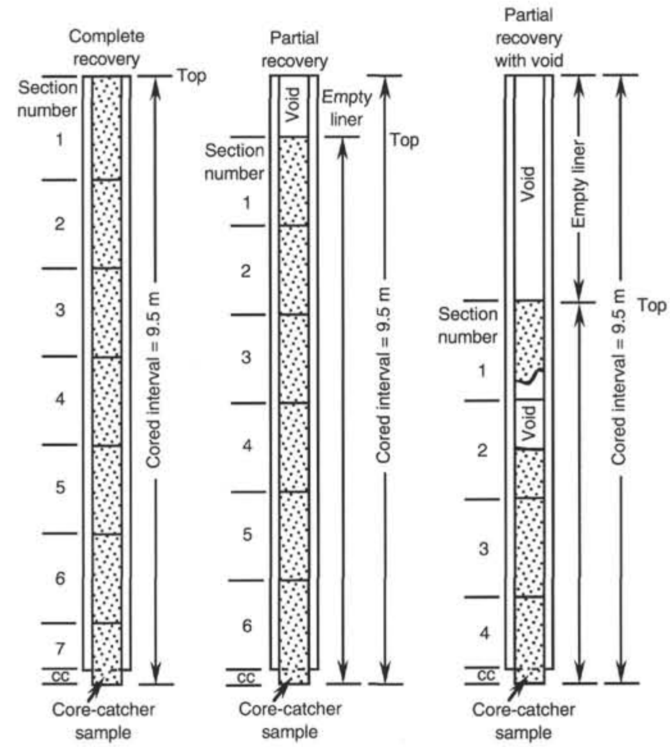

Figure 2. Examples of numbered core sections.

(Fig. 2). When full recovery is obtained, the sections are numbered from 1 through 7, with the last section generally being shorter than 1.5 m. Rarely, a core may require more than seven sections; this is usually the result of gas expansion having caused voids within some sections. When less than full recovery is obtained, as many sections as are needed to accommodate the length of the core will be recovered; for example, 4 m of core would be divided into two 1.5-m sections and a 1-m section. If cores are fragmented (recovery less than 100%), sections are numbered serially and intervening sections are noted as void, whether shipboard scientists think that the fragments were contiguous in situ or not. In rare cases, a section less than 1.5 m may be cut to preserve features of interest. Sections less than 1.5 m in length are also sometimes cut when the core liner is severely damaged.

By convention, material recovered from the core catcher is placed immediately below the last section when the core is described and is labeled core catcher (CC); in sedimentary cores, it is treated as a separate section. The core catcher is assigned the depth of the top of the cored interval in cases where material is only recovered in the core catcher (this convention differs from that used in the early days of deep-sea drilling), although information from the driller or other sources may indicate from what depth it was actually recovered.

When the recovered core is shorter than the cored interval, the top of the core is equated with the top of the cored interval by convention, to achieve consistency when handling analytical data derived from the cores. Samples removed from the cores are designated by distance, measured in centimeters from the top of the section to the top and bottom of each sample removed from that section. A complete identification number for a sample consists of the following information: leg, site, hole, core number, core type, section number, piece number (for hard rock), and interval in centimeters, measured from the top of section. For example, a sample identification of "154-925B-15H-6, 10–12 cm," would be interpreted as representing a sample removed from the interval between 10 and 12 cm below the top of Section 6, Core 15 (H designates that this core was taken by the advanced piston corer) of Hole 925B during Leg 154. Table 4 in the "Site 925" chapter (this volume) gives the depth of the top of "154-925B-15H-6" as 135.5 mbsf, so this sample would be placed at 135.60–135.62 mbsf. A computer routine was available to calculate depth in meters below seafloor (mbsf) from any correctly formulated ODP sample designation; this avoids inconsistencies that frequently arise on those occasions where some sections were cut to nonstandard lengths. Although depth in mbsf is an invaluable convention, it is not ideal, especially for high-resolution work (for composite depths, see below).

All ODP core and sample identifiers indicate core type. The following abbreviations are used: R = rotary core barrel (RCB), H = hydraulic piston core (HPC; also referred to as APC, or advanced hydraulic piston core), P = pressure core barrel, X = extended core barrel (XCB), B = drill-bit recovery, C = center-bit recovery, I = in situ water sample, S = sidewall sample, W = wash-core recovery, and M = miscellaneous material. APC, XCB, RCB, and W cores were cut during Leg 154.

Core Handling

As soon as a core was retrieved on deck, a sample taken from the bottom of the core catcher was given to the paleontological laboratory for an initial age assessment. Special care was taken in transferring the core from the drill floor to a long horizontal rack on a catwalk near the core laboratory so that the core did not bend or twist excessively. The core was capped immediately, and gas samples were taken by piercing the core liner and withdrawing gas into a vacuum tube. Voids within the core were sought as sites for gas sampling. Some of the gas samples were stored for shore-based study, but others were analyzed immediately as part of the shipboard safety and pollution-prevention program. Next, the core was marked into section lengths of 150 cm, each section was labeled, and the core was cut into sections. Interstitial-water (IW) and whole-round physical properties (PP) samples were also taken at this time. In addition, some headspace gas samples were taken from the end of cut sections on the catwalk and sealed in glass vials for light hydrocarbon analysis. Afterward, each section was sealed at the top and bottom by gluing on color-coded plastic caps: blue to identify the top of a section and clear for its bottom. A yellow cap was placed on section ends from which a whole-round sample was removed. The caps were usually attached to the liner by coating the end liner and the inside rim of the cap with acetone and then attaching the caps to the liners.

The cores were then carried into the laboratory, where the sections were labeled with an engraver to mark the complete designation of the section permanently. The length of the core in each section and the core-catcher sample were measured to the nearest centimeter. This information was logged into the shipboard CORELOG database program.

Whole-round sections normally were run through the multisensor track (MST). The MST includes the gamma-ray attenuation porosity evaluator (GRAPE), the *P*-wave logger, a volume magnetic susceptibility meter and a natural gamma emission detector. The core-catcher sample is not usually run through the MST track; thus, where possible we avoided using it for final biostratigraphic work. After the core had equilibrated to room temperature (approximately 3 hr), soft sediments were measured for thermal conductivity before being split. Cores were split lengthwise into working and archive halves. Softer cores were split with a wire. Harder cores were split using a diamond saw. The wire-cut cores were split from the top to bottom so that sediment below the voids or soupy intervals that were sometimes present at the top of Section 1 would not be drawn into the voids.

After splitting, working and archive halves of each section were designated. Archive halves were described visually. Smear slides were made from samples taken from the archive half. This was followed by passing the archive half of the core through the cryogenic magnetometer. Finally, the cores were photographed with both black-and-white and color film, a whole core at a time. Close-up photographs (black-and-white) were taken of particular features, as requested by individual scientists, for illustrations in the summary of each site.

The working half of the core was measured first for sonic velocity and vane shear strength. After physical properties sampling, the working half was sampled for reconnaissance-level and low-resolution shipboard and shore-based laboratory studies. Most sampling for detailed high-resolution paleoceanographic and paleoclimatic studies was deferred until after the cruise to optimize this sampling with the stratigraphic information obtained from biostratigraphy, paleomagnetic stratigraphy, and lithologic correlations.

Each sample taken either for shipboard or shore-based analysis was logged into the sampling data-base program by the location and the name of the investigator receiving the sample. Records of all of the samples removed are kept by the curator at ODP headquarters. The extracted samples were sealed in plastic vials or bags and labeled. Samples were routinely taken for shipboard physical properties analysis. These samples were subsequently used for calcium carbonate (coulometric) and organic carbon (CNS elemental) analyses; these data are reported in the site chapters.

Both halves of the core were placed into labeled plastic tubes, which were then sealed and transferred to cold-storage space aboard the drilling vessel. At the end of the leg, the cores were transferred from the ship in refrigerated air-freight containers to cold storage at the Bremen Core Repository.

LITHOSTRATIGRAPHY

Visual Core Description

Sediment "Barrel Sheets"

The core description forms (Fig. 3), or "barrel sheets," summarize the data obtained during shipboard analysis of each sediment core. The following discussion explains the ODP conventions used for compiling each part of the core description forms and the exceptions to these procedures adopted by the Leg 154 Shipboard Scientific Party.

Shipboard sedimentologists were responsible for visual core logging, smear-slide analyses, thin-section descriptions, color analysis, and grain-size analysis. Biostratigraphic (age), geochemical ($CaCO_3$, pore-water chemistry), physical properties (wet bulk density and shear strength), and X-ray diffraction (XRD) and fluorescence (XRF) data were integrated with sedimentological information to augment the visual core descriptions.

In addition to the sedimentological information on the barrel sheets, plots of the magnetic susceptibility, digital color reflectance spectroscopy, and natural gamma emission data (when determined) are displayed next to the traditional barrel sheet information (Fig. 3).

Core Designation

Cores are designated using leg, site, hole, core number, and core type as discussed in a preceding section (see "Numbering of Sites, Holes, Cores, and Samples" section, this chapter). The cored interval is specified in terms of meters below seafloor (mbsf). When necessary for inter-hole and/or inter-site comparison, lithostratigraphic data are presented vs. meters composite depth (mcd; see "Composite Depths" section, this chapter).

Graphic Lithology Column

The lithology of the material recovered is represented on the core description forms by up to three symbols in the column titled "Graphic Lithology" (Figs. 3 and 4). Where an interval of sediment or sedimentary rock is a homogeneous mixture, the constituent categories have been separated by a solid vertical line, with each category represented by its own symbol. Constituents accounting for <10% of the sediment in a given lithology are not shown in the "Graphic Lithology" column. In an interval comprising two or more sediment lithologies that have different compositions, and which are thinly interbedded, the average relative abundances of the lithologic constituents are represented graphically by dashed lines that vertically divide the interval into appropriate fractions, as described above. The "Graphic Lithology" column shows only the composition of layers or intervals exceeding 20 cm in thickness.

Chronostratigraphy

The chronostratigraphic unit, as recognized on the basis of paleontological results, is shown in the "Age" column. The zonations and ages used during Leg 154 are presented in the "Biostratigraphy" section (this chapter).

Sedimentary Structures

In sediment cores, natural structures and deformation structures created by the coring process can be difficult to distinguish. Natural structures observed are indicated in the "Structure" column of the core description form. The column is divided into three vertical areas for symbols. The intensity of bioturbation is shown in the central portion of the "Structure" column of the barrel sheet in the conventional manner (slight, moderate, heavy). The symbols on either side of the "Structure" column indicate the location of individual bedding features, thin color banding, and any other sedimentary features (e.g., nodules, disseminated pyrite, and discrete trace fossils, such as *Zoophycos*). The symbols used to describe each of these primary and secondary biogenic and physical sedimentary structures are shown in Figure 5.

Sedimentary Disturbance

Sediment disturbance resulting from the coring process is illustrated in the "Disturbance" column on the core description form (using symbols in Fig. 5). Blank regions indicate an absence of drilling disturbance. The degree of drilling disturbance is described for soft and firm sediments using the following categories:

1. Slightly disturbed: bedding contacts are slightly deformed.
2. Moderately disturbed: bedding contacts have undergone extreme bowing.

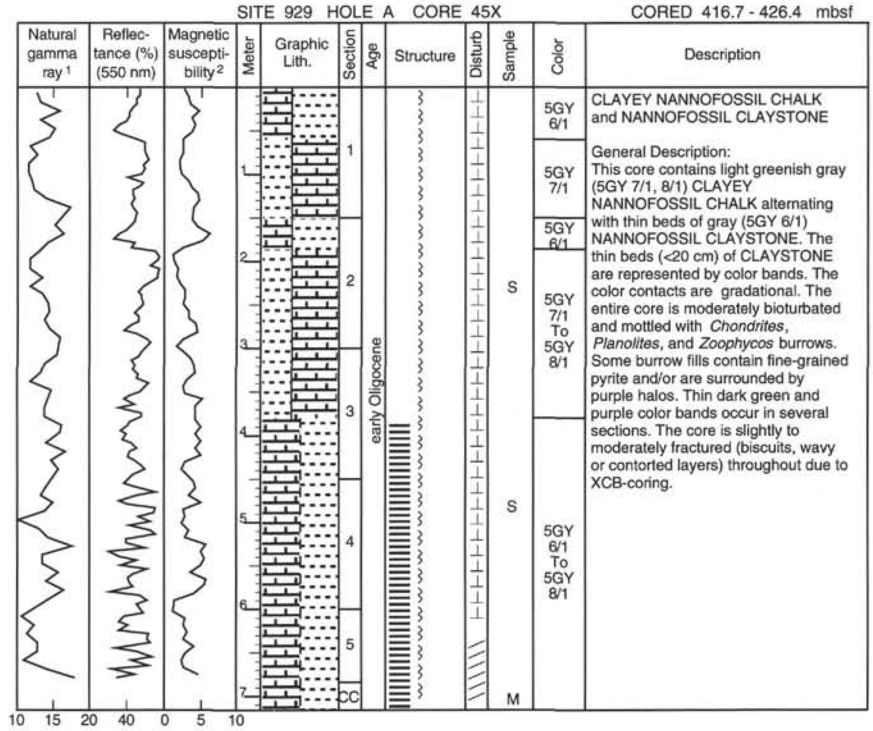

Figure 3. Example of a core description form (barrel sheet) used for sediments and sedimentary rocks on Leg 154.

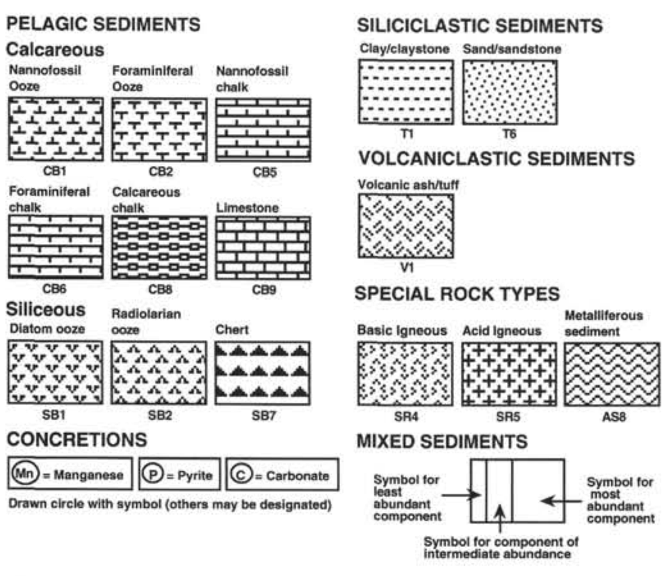

Figure 4. Key to symbols used in the "Graphic Lithology" column of the core description forms.

3. Highly disturbed: bedding is completely deformed as flow-in, coring/drilling slough, and other soft sediment stretching and/or compressional shearing structures attributed to the coring/drilling process.

4. Soupy: intervals are water-saturated and have lost all aspects of original bedding.

The degree of fracturing in indurated sediments and igneous rocks is described using the following categories:

1. Slightly fractured: core pieces are in place and broken.

2. Moderately fractured: core pieces are in place or partly displaced, and original orientation is preserved or recognizable (drilling slurry may surround fragments, i.e., drilling/coring "biscuits" are evident).

3. Highly fractured: core pieces are from the interval cored and probably in the correct stratigraphic sequence (although they may not represent the entire section), but original orientation is completely lost.

4. Drilling breccia: core pieces have lost their original orientation and stratigraphic position and may be mixed with drilling slurry.

Samples

The position of samples taken from each core for shipboard analysis is indicated in the "Samples" column on the core description form ("barrel sheet"; see Fig. 3). The symbol "S" indicates the location of smear-slide samples, the symbol "T" indicates the location of thin-section samples, and the symbol "M" indicates the location of paleontology samples. The notations "I" and "P" designate the location of samples for whole-round interstitial water geochemistry and physical properties analyses, respectively.

Color

The hue and chroma attributes of color were determined using the Minolta CM-2002 hand-held Spectrophotometer as soon as possible after the cores were split, because redox-associated color changes may occur when deep-sea sediments are exposed to the atmosphere. Core color, in standard Munsell notation (Munsell, 1975), is given in the "Color" column on the core description form. The CM-2002 color scanner was also used to measure reflected visible light in 31, 10-nm-wide bands ranging from 400 to 700 nm. These reflectance measurements were taken at 5-cm intervals on all cores except for Hole 925A, which was measured at 10-cm intervals. To protect the spectrophotometer, wet and unconsolidated cores were wrapped before measuring; Appendix A gives the correction factors associated with the transparent wrapping. On the barrel sheets, reflectance at 550 nm is plotted.

Lithologic Description—Text

The lithologic description that appears on each core description form (barrel sheet) consists of three parts: (1) a heading that lists all the major sediment lithologies observed in the core; (2) a general description of these sediments, including location in the core of

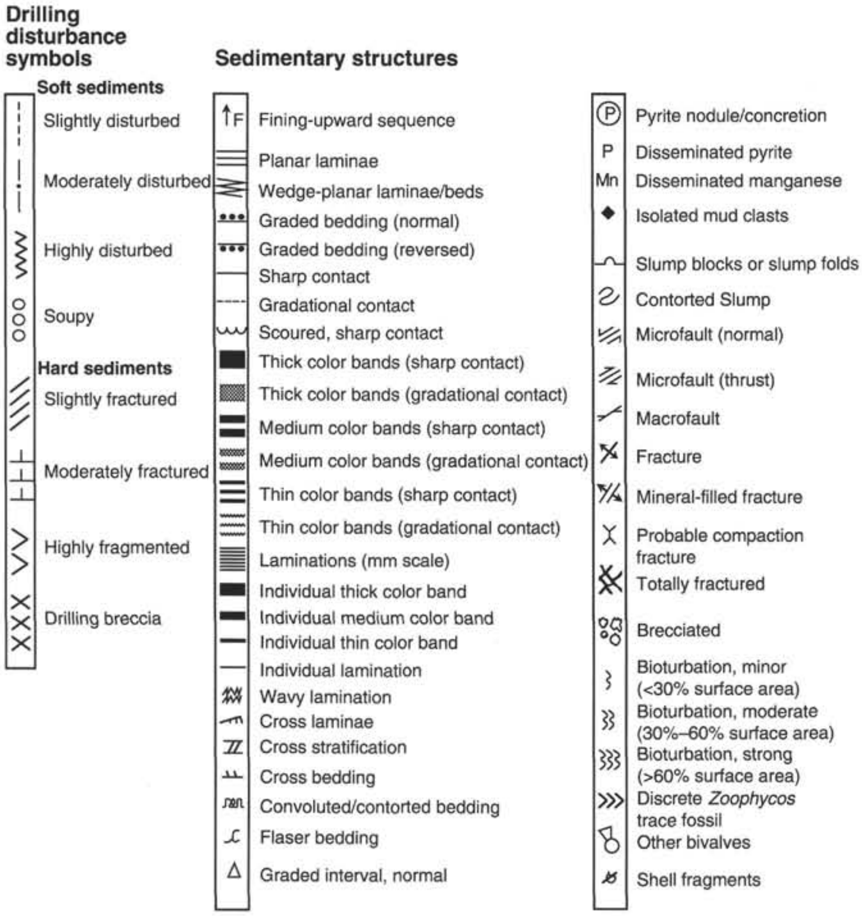

Figure 5. Symbols used for the "Disturbance" column of the core description forms, and symbols used to indicate color banding, bioturbation, and isolated sedimentary structures/trace fossils/macrofossils columns in the "Structure" column of the core description forms.

significant features; and (3) a subjective index of the contrast in color banding in the core. Descriptions and locations of thin, interbedded, or minor lithologies are included in the text as well as any clarifying information regarding sediment disturbance produced by natural processes or by the drilling/coring process.

Smear-slide Summary

A table summarizing data from smear-slide and thin-section analyses is included in the CD-ROM for this *Initial Reports* volume. This table includes information about the sample location, whether the sample represents a dominant ("D") or a minor ("M") lithology in the core, and the estimated percentages of sand, silt, and clay, together with all identified components. The subjective nature of these data should be kept in mind. In all cases, clay mineral content had to be estimated with the aid of carbonate data and color data.

Sedimentology

Classification of Sediments and Sedimentary Rocks

We have followed the classification procedures suggested by Mazzullo et al. (1988). The sediments on Leg 154 are composed of pelagic and siliciclastic components according to this classification scheme. The pelagic component is composed of the skeletal debris of open-marine calcareous and, to a lesser extent, siliceous microfauna (e.g., foraminifers and radiolarians) and microflora (e.g., calcareous nannofossils and diatoms) and associated organisms. The siliciclastic component is composed of mineral and rock fragments that were derived from igneous, sedimentary, and metamorphic rocks, and which consist mainly of clay minerals for Leg 154. The relative proportions of the two components are used to define the major classes of "granular" sediments encountered. Thus, pelagic sediments are composed of >60% biogenic grains, and siliciclastic sediments are composed of >60% siliciclastic grains (Mazzullo et al., 1988). Mixed sediments contain proportions of these two grain types between 40% and 60%.

Classification of Granular Sediment

A granular sediment may be classified by designating a principal name and major and minor modifiers (Mazzullo et al., 1988). The principal name of a granular sediment defines its granular sediment class; the major and minor modifiers describe the texture, composition, fabric, and/or shape of the grains themselves (Table 1).

Principal Names

Each granular sediment class has a unique set of principal names, which are outlined in Table 1.

For pelagic sediment, the principal name describes the composition and degree of consolidation using the following terms:

1. Ooze: unconsolidated calcareous and/or siliceous biogenic sediments.
2. Chalk: firm biogenic sediment composed predominantly of calcareous biogenic grains with shear strengths >200 kPa.
3. Limestone: hard pelagic sediment composed predominantly of calcareous pelagic grains.

For siliciclastic sediment, the principal name describes the texture and is assigned according to the following guidelines:

1. The Udden-Wentworth grain-size scale (Wentworth, 1922) defines the grain-size ranges and the names of the textural groups

(gravel, sand, silt, and clay) and subgroups (fine sand, coarse silt, etc.) that are used as the principal names of siliciclastic sediment.

2. When two or more textural groups or subgroups are present in a siliciclastic sediment, they are listed as principal names in order of increasing abundance.

3. The suffix "stone" is affixed to the principal names sand, silt, and clay when the sediment is lithified.

Major and Minor Modifiers

The principal name of a granular sediment class is preceded by major modifiers and is followed by minor modifiers (preceded by the term "with") that describe the lithology of the granular sediment in greater detail (Table 1). The most common use of major and minor modifiers is to describe the composition and textures of grain types that are present in major (>25%) and minor (10% to 25%) proportions. Note that modifiers are always listed in order of increasing abundance. As an example, an unconsolidated pelagic sediment containing 30% clay, 15% foraminifers, and 55% nannofossils would be called a clayey nannofossil ooze with foraminifers (Mazzullo et al., 1988).

BIOSTRATIGRAPHY

Introduction

Preliminary age assignments were based on biostratigraphic analyses of calcareous nannofossils and planktonic foraminifers. Stratigraphic constraint of calcareous nannofossil datums was achieved by examining one to six samples per section of core (a sample spacing of 1.5 to 0.25 m). Constraint on planktonic foraminifer datums in those stratigraphic intervals that were multiply cored was achieved by examining three to six samples per core (a sample spacing of 3 to 1.5 m). For stratigraphic intervals recovered in a single hole, between one and six samples per 9.5 m core were studied.

Most previous shipboard studies of planktonic foraminifers have been limited to core-catcher samples by time constraints. We achieved a greater sampling density for those intervals that were multiply cored by using the method previously adopted during Leg 138 (Mayer, Pisias, Janecek, et al., 1992); that is, by concentrating efforts on one of the three APC holes. Hole-to-hole correlations were achieved mainly through the use of the data provided by the multisensor track (see "Composite Depths" section, this chapter). This method, as opposed to examination of core-catcher samples from all holes at a site, enabled us to attain more precise shipboard biostratigraphy.

The abundance, preservation, and zonal assignment for each sample are recorded in the stratigraphic site summary sheets.

Age estimates of nannofossil and planktonic foraminifer datums that were not already published on the Leg 154 time scale (this chapter) were converted to it from ages estimated on the time scale of Berggren et al. (1985a, 1985b), either through linear interpolation between the nearest geomagnetic reversal boundaries in the sites where they were best calibrated, or by interpolation using other datums that had already been expressed on our time scale. This enabled us to convert ages that were based on the polarity scale of Berggren et al. (1985a, 1985b) to that used here (see "Paleomagnetism" section, this chapter). The Pliocene/Pleistocene and Miocene/Pliocene boundaries are considered well constrained, from both a chronostratigraphic and chronologic point of view (Rio et al., 1991, in press). The chronostratigraphy and chronology of the three remaining, older, Cenozoic epoch boundaries remain controversial. We converted the estimates of Berggren et al. (1985a, 1985b) for the Oligocene/Miocene, the Eocene/Oligocene, and the Cretaceous/Tertiary boundaries.

We subdivided the Pliocene into three standard stages, in accordance with Rio et al. (1991). The middle Pliocene (Piacenzian) occupies the interval from the top of the *Reticulofenestra pseudoumbilicus* Zone (CN11/CN12 boundary) at 3.77 Ma to the Gauss/Matuyama boundary at 2.60 Ma. The late Pliocene (the Gelasian Stage; Rio et al., in press), therefore, encompasses the interval from the onset of the Matuyama to the termination of the Olduvai at 1.77 Ma.

Our placement of the Paleocene/Eocene (P/E) boundary requires some discussion. Berggren et al. (1985a) placed the P/E boundary at the nannofossil NP9/NP10 zonal boundary, which is defined by the first appearance of *Tribrachiatus bramlettei* (Martini, 1971). Aubry et al. (1988) suggested that the P/E boundary should fall within Zone NP10, rather than at its base. Berggren et al. (1985a) and Aubry et al. (1988, p. 735), however, approximated the base of NP10 with the extinction of the nannofossil genus *Fasciculithus* (i.e., *F. tympaniformis*). This event occurred about 0.2 m.y. before the appearance of *T. bramlettei,* according to the Leg 154 time scale (Table 2); that is, within the late part of Zone NP9.

Planktonic foraminifer workers have used the extinction level of *Morozovella velascoensis* to approximate the P/E boundary (e.g., Berggren et al., 1985a). This extinction corresponds to the Zone P5/P6 boundary in the zonation used here (this chapter). Recently, Bralower et al. (in press) demonstrated from the tropical Pacific Site 865 that the extinction of *M. velascoensis* occurred within the range of the *T. bramlettei*–*T. contortus* lineage; that is, within Zone NP10. From the data that Bralower et al. (in press) presented, we have estimated an age of 53.4 Ma for the *M. velascoensis* extinction using linear interpolation between the appearance of *Discoaster lodoensis* at 52.0 Ma and the appearance of *Discoaster multiradiatus* at 56.3 Ma. We used the *M. velascoensis* datum as an approximation for the P/E boundary.

Calcareous Nannofossils

During Leg 154, we referred to the zonal scheme of Bukry (1973, 1975; see also Bukry, 1978, for a summary), code numbered by Okada and Bukry (1980). This zonation is regarded as a general framework for the biostratigraphic classification of low-latitude Cenozoic marine sediments based on calcareous nannofossils. Bukry's Cenozoic zonal scheme is presented in Figure 6, together with the geomagnetic polarity time scale (see "Paleomagnetism" section, this chapter). Martini's (1971) nannofossil zonation is also shown, for reference.

Cenozoic biostratigraphic events, including Okada and Bukry's (1980) zonal indicators, are listed in Table 2. The events have been tied directly to magnetostratigraphic records, many of which are derived from extra-tropical environments. This is particularly true for the Paleogene events. Note that more than one datum event may be associated with a given zonal/subzonal boundary (e.g., CN8b). This indicates that Bukry used two datum events for its definition. A few of Okada and Bukry's zones or subzones are not accounted for in Table 2 (e.g., CN11). This generally indicates events that we consider inadequately correlated to the magnetostratigraphic record. Questionable placement of the base of CN14a and the base of CN13b arise from taxonomic ambiguities.

Methods

Calcareous nannofossils were examined by means of standard light microscope techniques, under crossed nicols and transmitted light at 1000× magnification.

A peculiar characteristic among calcareous nannofossil assemblages is that individual samples may show signs of strong etching as well as strong overgrowth; more dissolution-resistant forms apparently accrete calcite provided by dissolution of other forms. Qualitative descriptions of calcareous nannofossil preservational states commonly involve a sophisticated code system that accounts for dissolution and overgrowth on a progressive scale (e.g., Roth and Thierstein, 1972). We have adopted a simple, but effective, code system to characterize preservational states. Thus, preservation was recorded as follows:

G = good (little or no evidence of dissolution and/or secondary overgrowth of calcite; diagnostic characters fully preserved);
M = moderate (dissolution and/or secondary overgrowth; partially altered primary morphological characteristics; however, nearly all specimens can be identified at the species level); and

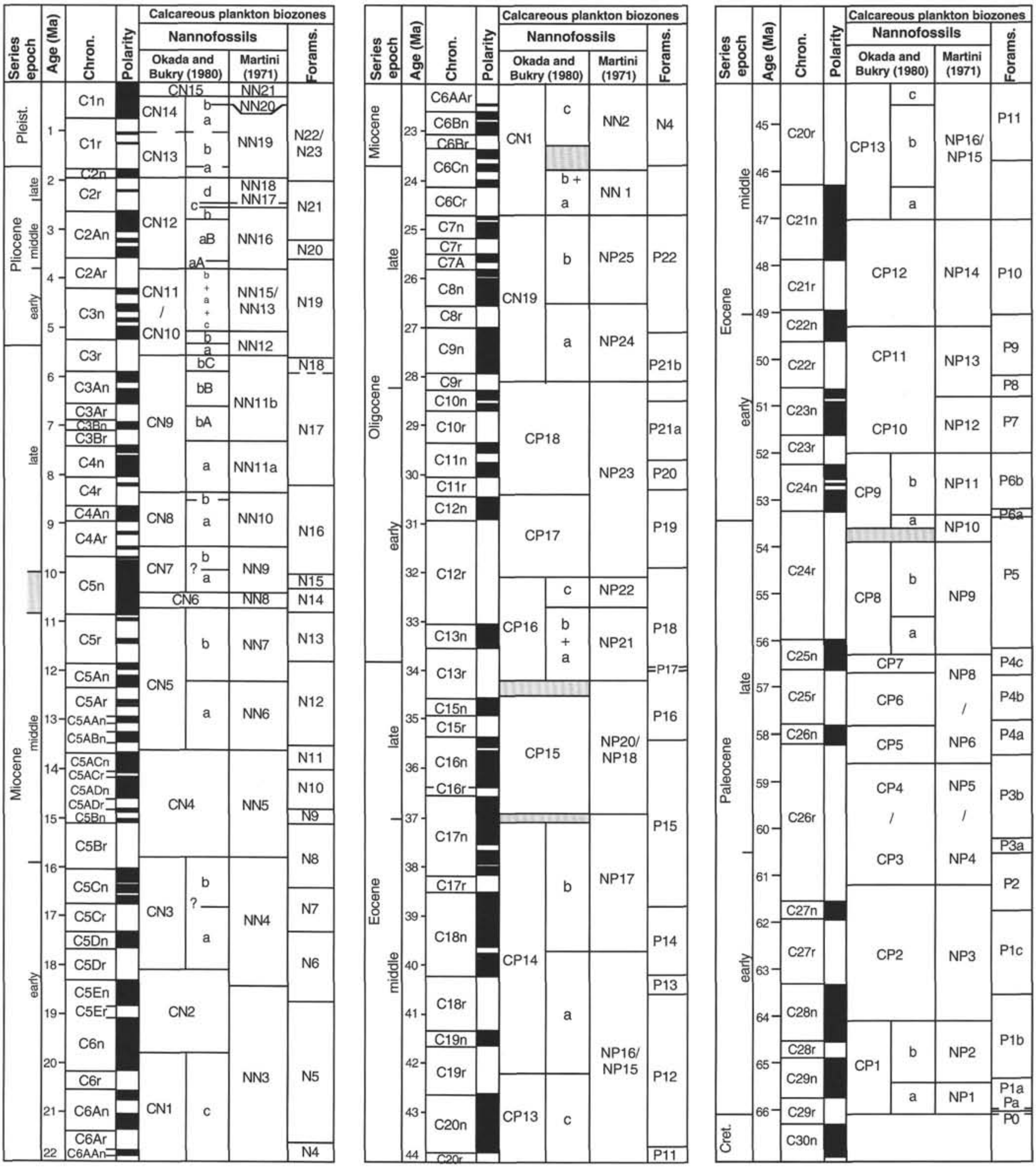

Figure 6. Correlation chart for the interval from 0 to 66 Ma.

P = poor (severe dissolution, fragmentation, and/or secondary overgrowth with primary features largely destroyed; many specimens cannot be identified at the species level and/or generic level).

Five levels of relative abundance were recorded as follows:

A = abundant (the taxonomic category constitutes >10% of the total assemblage);

C = common (the taxonomic category constitutes from 1% to 10% of the total assemblage);

F = few (the taxonomic category makes up from 0.1% to 1% of the total assemblage);

R = rare (the taxonomic category makes up from <0.1% of the total assemblage); and

B = barren.

Table 1. Outline of the sediment classification scheme used by Mazzullo et al. (1988) for pelagic and siliciclastic sediments and sedimentary rocks.

Sediment class	Major modifier	Principal names	Minor modifiers
Pelagic	1. Composition of biogenic and neritic grains present in major amounts. 2. Texture of clastic grains present in major amounts.	1. Ooze 2. Chalk 3. Limestone 4. Radiolarite 5. Diatomite 6. Spiculite 7. Chert	1. Composition of biogenic grains present in minor amounts. 2. Texture of clastic grains present in minor amounts.
Siliciclastic	1. Composition of all grains present in major amounts. 2. Grain fabric (gravels only) 3. Grain shape (optional) 4. Sediment color (optional)	1. Gravel 2. Sand 3. Silt 4. Clay (etc.)	1. Composition of all grains present in minor amounts. 2. Texture and composition of siliciclastic grains present as matrix (for coarse-grained clastic sediment).

Table 2. Age estimates of calcareous nannofossil datum events.

Event	Zone (base)	Age (Ma)	Reference
B Acme *Emiliania huxleyi*		0.085	1
B *Emiliania huxleyi*	CN15	0.26	1
T *Pseudoemiliania lacunosa*	CN14b	0.46	1
Reentrance medium *Gephyrocapsa* spp.	CN14a?	1.03	2
T Large *Gephyrocapsa* spp.		1.24	2
B Large *Gephyrocapsa* spp.		1.46	2
T *Helicosphaera sellii*		1.47	2
T *Calcidiscus macintyrei*		1.60	2
B Medium *Gephyrocapsa* spp.	CN13b?	1.67	2
Pleistocene/Pliocene boundary		1.77	
T *Discoaster brouweri*	CN13a	1.95	2
B Acme *Discoaster triradiatus*		2.15	2
T *Discoaster pentaradiatus*	CN12d	2.44	3
T *Discoaster surculus*	CN12c	2.61	3
T *Discoaster tamalis*	CN12b	2.76	3
T *Sphenolithus* spp.	CN12aB	3.62	3
T *Reticulofenestra pseudoumbilicus*	CN12aA	3.77	3
T *Ceratolithus acutus*		5.04	**
B *Ceratolithus rugosus*	CN10c	5.04	3
B *Ceratolithus acutus*	CN10b	5.34	4
T *Triquetrorhabdulus rugosus*		5.34	4
Pliocene/Miocene boundary		5.38	
T *Discoaster quinqueramus*	CN10a	5.56	4
T *Amaurolithus amplificus*	CN9bC	5.88	4
B *Amaurolithus amplificus*	CN9bB	6.5	4
T Paracme *R. pseudoumbilicus*		6.8	4
B *Amaurolithus primus*	CN9bA	7.3	4
Bc *Discoaster surculus*		7.8	4
B *Discoaster berggrenii*	CN9a	8.4	4
B Paracme *R. pseudoumbilicus*		8.8	4
T *Catinaster calyculus*		9.36	**
T *Discoaster hamatus*	CN8a	9.4	4
B *Minylitha convallis*		9.4	4
B *Discoaster neohamatus*		9.6	4
B *Discoaster hamatus*	CN7	10.4	4
B *Catinaster coalitus*	CN6	10.7	4
T *Coccolithus miopelagicus*		10.8	**
Tc *Discoaster kugleri*		11.3	4
Bc *Discoaster kugleri*		11.7	4
T *Coronocyclus nitescens*		12.1	4
B *Discoaster kugleri*	CN5b	12.2	4
B *Calcidiscus macintyrei* ≥11 µm		12.3	4
B *Triquetrorhabdulus rugosus*		12.6	4
T *Calcidiscus premacintyrei*		12.7	4
T *Discoaster signus*		12.7	4
Tc *Cyclicargolithus floridanus*		13.2	4
T *Sphenolithus heteromorphus*	CN5a	13.6	4
T *Helicosphaera ampliaperta*	CN4	15.8	5
B *Discoaster signus*		16.2	4
T Abundant *Discoaster deflandrei*		16.2	4
B *Calcidiscus premacintyrei*		17.4	6
B *Sphenolithus heteromorphus*	CN3	18.1	7
T *Sphenolithus belemnos*		18.4	7
B *Sphenolithus belemnos*	CN2	19.7	7
T *Triquetrorhabdulus carinatus*		23.1	7
B *Discoaster druggi*	CN1c	23.3	8
T Acme *Sphenolithus delphix*		23.7	9
Miocene/Oligocene boundary		23.8	
T *Dictyococcites bisectus*	CN1c	23.8	10
B Acme *Sphenolithus delphix*		24.4	9
T *Sphenolithus ciperoensis*	CN1a	24.7	11
T *Sphenolithus distentus*	CP19b	26.5	11
T *Sphenolithus predistentus*		27.4	11
B *Sphenolithus ciperoensis*	CP19a	28.1	11
B *Sphenolithus distentus*	CP18	30.4	11
T *Reticulofenestra umbilicus*	CP17	32.1	10
T *Coccolithus formosus*	CP16c	32.7	12
Oligocene/Eocene boundary		33.8	
T *Discoaster saipanensis*	CP16a	34.2	12
T *Discoaster barbadiensis*	CP16a	34.5	12
T *Cribrocentrum reticulatum*		35.0	12
T *Calcidiscus protoannulus*		35.4	12
B *Chiasmolithus oamaruensis*	CP15	36.9	10
T *Chiasmolithus grandis*	CP15	37.1	10
T *Chiasmolithus solitus*	CP14b	39.7	10
B *Dictyococcites hesslandii*		40.4	12
T *Nannotetrina* spp.		41.9	12
B *Reticulofenestra umbilicus* ≥14µm	CP14a	42.2	12
T *Chiasmolithus gigas*	CP13c	44.6	10
B *Chiasmolithus gigas*	CP13b	46.3	13
B *Nannotetrina fulgens*	CP13a	47.0	13
T *Discoaster sublodoensis*		47.2	13
B *Nannotetrina* spp.		47.8	13
T *Discoaster lodoensis*		47.9	13
B *Discoaster sublodoensis*	CP12	49.3	13
T *Tribrachiatus orthostylus*		50.8	13
B *Discoaster lodoensis*	CP10	52.0	13
T *Sphenolithus radians*		53.1	13
Transition *T. contortus–T. orthostylus*	CP9b	53.3	13
Eocene/Paleocene boundary		53.4	
B *Tribrachiatus contortus*	CP9a	53.6	13
B *Tribrachiatus bramlettei*		53.9	13
B *Discoaster diastypus*	CP9a	53.9	13
B *Rhomboaster* spp.		54.0	13
T *Fasciculithus* spp.		54.1	13
T *Ericsonia robusta*		55.1	13
B *Campylosphaera eodela*	CP8b	55.5	10
B *Discoaster multiradiatus*	CP8a	56.3	13
B *Discoaster okadai*		56.6	13
B *Discoaster nobilis*	CP7	56.7	13
T *Heliolithus kleinpellii*		57.7	13
B *Discoaster mohleri*	CP6	57.8	13
T *Chiasmolithus danicus*		58.6	10
B *Heliolithus kleinpellii*	CP5	58.6	13
B *Heliolithus cantabriae*		59.3	13
T *Fasciculithus pileatus*		59.7	13
T *Cruciplacolithus tenuis*		59.7	10
B *Fasciculithus* spp.		60.3	13
B *Ellipsolithus macellus*	CP3	61.2	13
B *Sphenolithus* spp.		61.4	13
B *Chiasmolithus bidens*		61.7	10
B *Chiasmolithus danicus*	CP2	64.1	10
B *Cruciplacolithus tenuis*	CP1b	65.4	10
B *Cruciplacolithus primus*		65.7	10
B *Biantholithus sparsus*		66.1	10
T Cretaceous taxa	CP1a	66.1	10
Tertiary/Cretaceous boundary		66.1	

Note: B = base, T = top, Bc = base common occurrence, and Tc = top common occurrence. References are as follows: 1 = Thierstein et al. (1977), 2 = Raffi et al. (1993), 3 = Backman and Shackleton (1983), 4 = Raffi and Flores (in press), 5 = Backman et al. (1990), 6 = Gartner (1992), 7 = Olafsson (1991), 8 = Berggren et al. (1985a), 9 = Fornaciari et al. (1990), 10 = Berggren et al. (1985b), 11 = Olafsson and Villa (1992), 12 = Backman (1987), 13 = Backman (1986), and double asterisk (**) = Site 925.

Planktonic Foraminifers

Zonation

The tropical Neogene planktonic foraminifer "N-zonation" scheme used here follows Blow (1969), as modified by Kennett and Srinivasan (1983) and used during various recent ODP legs (e.g., Chaisson and Leckie, 1993; Leckie et al. 1993). The following minor modifications were made:

1. Zone N4 was not subdivided because doubt has been cast on the reliability of the first occurrence (FO) of *Globoquadrina dehiscens* for correlation outside of the Pacific. Premoli Silva and Spezzaferri (1990) and Spezzaferri and Premoli Silva (1991) found the FO of *G. dehiscens* in Zone P22 in the Indian Ocean and Gulf of Mexico, respectively.
2. Kennett and Srinivasan (1983) subdivided Blow's Zone N17 using the FO of *Pulleniatina primalis.* This partition was not employed during Leg 154 because of the irregular stratigraphic occurrence of *Pulleniatina primalis* in Caribbean and Atlantic sediments (Bolli and Saunders, 1985).
3. As early as 1973, Bolli and Premoli Silva questioned the stability of the *Globorotalia truncatulinoides* datum at 2.0 Ma. Much of the problem stems from the difficulty of separating *G. truncatulinoides* from its presumed ancestor, *G. tosaensis* (Kennett and Srinivasan, 1983). The "*truncatulinoides*" morphotype can no longer be considered a good approximation for the Pliocene/Pleistocene boundary. However, it is not found below the FO of *G. tosaensis* and, therefore, can still be used as a datum for the base of Zone N22.
4. Both Bolli and Premoli Silva (1973) and Blow (1979) recognized the FO of "*Globigerina*" *calida calida* as a zone boundary. Bolli and Premoli Silva (1973) cited an age of 0.14 Ma, but no basis for the age estimate was provided. Zone N23, therefore, was not differentiated from Zone N22.

Ongoing research on the taxonomy and biostratigraphy of Paleogene planktonic foraminifers has necessitated the adoption of an unpublished Paleogene tropical-subtropical "P-zonation" that follows Berggren and Norris (1993) and Berggren et al. (in press). This zonation is a substantial modification of the one evolved by Berggren (1969), Berggren et al. (1985a), and Berggren and Miller (1988). In particular, the numbering system for zones in the Paleocene to early Eocene interval differs in several places from that given in Berggren and Miller (1988). The following modifications have been made by Berggren et al. (in press) and are summarized and compared with the "P-zonation" of Berggren and Miller (1988) and Blow (1979) in Figure 7:

1. Zone Pα of Berggren and Miller (1988) has been modified and divided into Zones P0 and Pa. Zone P0 is the interval between the last occurrence (LO) of *Globotruncana* spp. and the FO of *Parvularugoglobigerina eugubina* (see Keller, 1988). Zone Pa is the total range of *P. eugubina.* The LO of *P. eugubina* approximates the FO of *Parasubbotina pseudobulloides.*
2. In Berggren and Miller (1988), Zone P3 was divided into Subzones P3a and P3b by using the FO of "*Morozovella*" *pusilla,* which was thought to post-date the FO of *Morozovella angulata.* However, Berggren and Norris (1993) recorded a simultaneous FO of *M. angulata* and "*M.*" *pusilla,* which means that the original Subzone P3a of Berggren and Miller (1988) does not exist. Instead, Berggren et al. (in press) have divided Zone P3 into new Subzones P3a and P3b by the FO of "*Morozovella*" *albeari,* which is a carinate descendant of "*M.*" *pusilla* and is regarded as synonymous with "*M.*" *laevigata.*
3. Zone P4 of Berggren and Miller (1988) is unchanged, but it has been divided into three subzones by using the LO of *Acarinina subsphaerica* and the FO of *Acarinina soldadoensis.* Note that the latter biohorizon was used by Blow (1979) as the base of his Zone P5.
4. Zone P5 of Berggren and Miller (1988) is no longer thought to exist because an overlap in the ranges of *Globanomalina pseudomenardii* and *Morozovella subbotinae* has now been confirmed (cf. Blow 1979). To preserve numerical continuity, a new Zone P5 was defined by Berggren et al. (in press) that is equivalent to Subzone P6a of Berggren and Miller (1988), minus the short interval of overlap between *G. pseudomenardii* and *M. subbotinae.*
5. Zone P6 is amended as the interval from the LO of *Morozovella velascoensis* to the FO of *M. aragonensis.* The FO of *M. formosa* is used to subdivide the zone, so that Subzone P6a of Berggren et al. (in press) = Subzone P6b of Berggren and Miller (1988) = Zone P7 of Blow (1979), and Subzone P6b of Berggren et al. (in press) = Subzone P6c of Berggren and Miller (1988) = Subzone P8a of Blow (1979). Zones P7 through P22 of Berggren et al. (in press) are unchanged from Berggren and Miller (1988) but differ from the numerical coding of Blow (1979) (see discussions in Berggren and Miller, 1988).

A list of planktonic foraminifer datums used in this study is presented in Table 3, which mainly follows Berggren et al. (in press) and Berggren et al. (1985a, 1985b) with various modifications.

Methods

Sample preparation procedures varied according to the degree of lithification of the sample. Unlithified ooze was either washed directly in tap water or soaked briefly in a weak Calgon solution, then washed over 150- and 40-µm mesh sieves. Semilithified ooze was first partially broken up by hand and then soaked in a weak Calgon solution before washing and sieving. Chalk lumps were crushed and soaked in a hot Calgon solution before ultrasonic cleaning and a second soaking in weak Calgon solution before washing. All samples were dried at approximately 50°C on a hot plate.

The following abundance categories were estimated from a visual examination of the dried sample:

A = abundant (>30%);
C = common (15%–30%);
F = few (3%–15%);
R = rare (<3%); and
B = barren.

Preservation was estimated in the following categories:

G = good (>90% of the specimens unbroken; few signs of dissolution);
M = moderate (30%–90% of specimens broken or dissolved); and
P = poor (<30% of specimens intact).

Benthic Foraminifers

Benthic foraminifers were identified in samples from Leg 154 to determine past changes in water-mass distribution, one of several factors that control the abundance of these organisms. The taxa can be roughly divided into an Antarctic Bottom Water (AABW) assemblage, characterized by a high abundance of *Nuttallides umbonifera* and a North Atlantic Deep Water (NADW) assemblage, characterized by a high abundance of *Hoeglundina elegans, Cibicidoides wuellerstorfi,* and *Pyrgo* spp. (Schnitker, 1974, 1980; Lohmann, 1978; Corliss, 1979; Mackensen et al., 1993).

To obtain benthic foraminifers, samples were disaggregated and wet sieved through a 63-µm mesh. A coarser sieve was usually not used because several small species are important indicators of water mass. However, in case of rare abundance, washed samples were dry sieved through a 150-µm mesh. A variety of methods was used for disaggregation, including ultrasonic treatment, soaking in a hot Calgon solution, and soaking in hydrogen peroxide, where necessary. The sediments were dried under an infrared lamp and divided using

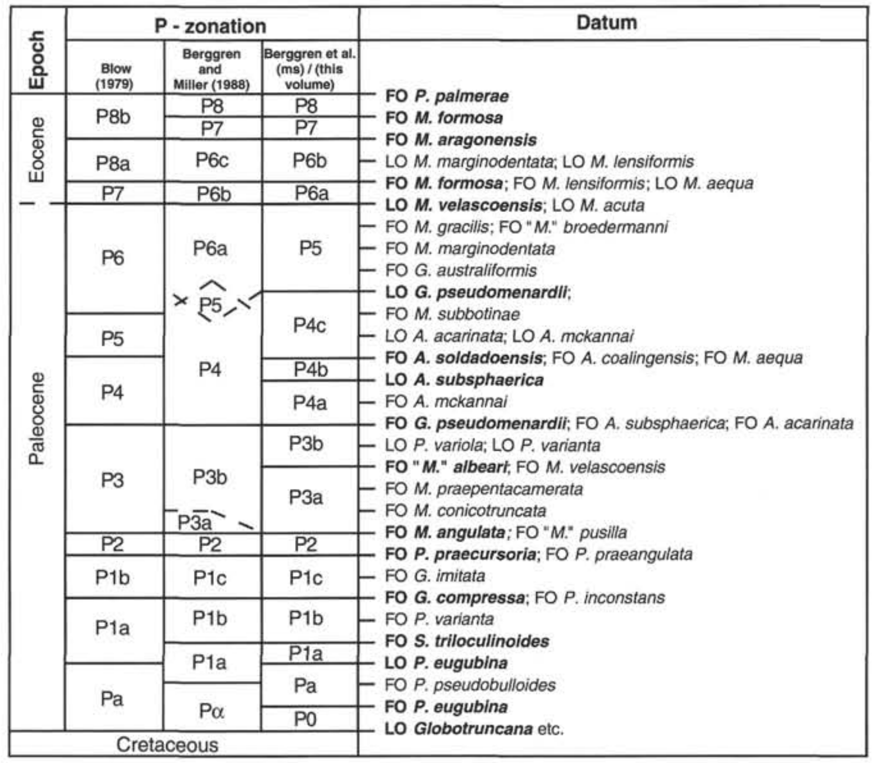

Figure 7. Paleocene and early Eocene planktonic foraminifer "P-zonation" used in this study, after Berggren et al. (in press), compared with the notations used by Blow (1979) and Berggren and Miller (1988). Datums used to define zonal and subzonal boundaries in this study are shown in bold text. The vertical scale does not represent absolute time.

a microsplitter. The foraminifers were identified under the binocular microscope.

Benthic species abundance categories are as follows: R (rare), <1%; F (few), 1%–5%; C (common), 5%–20%; and A (abundant), >20%. The preservation state of benthic foraminifer faunas is determined by the condition of the tests and the number of broken individuals. Preservation was categorized as follows: G (good), with more than 80% of the specimens unbroken; M (moderate), with 30%–80% of the specimens unbroken, and P (poor), with more than 70% of the specimens dissolved or broken.

Sedimentation Rates and Mass Accumulation Rates

Methods

To determine sedimentation rates, we first had to generate an age-depth relationship. At a site with precisely determined paleomagnetic stratigraphy and with unambiguously identified chrons, uncertainties in accumulation rates arise almost entirely from uncertainties in the reversal time scale. Where biostratigraphic datums are used, the chief uncertainty arises from the fact that with a limited amount of time available, many datums are determined between widely separated limits, and inconsistencies are frequent. During many ODP legs, it has been necessary to reconstruct sedimentation rates using datums determined only in core catchers (i.e., within 9.5 m). The uncertainty in each sedimentation rate estimate derived in this way is related to the thickness interval over which it is averaged, divided by the combined uncertainty in the top and bottom controls. At a sedimentation rate of 20 m/m.y., datums spaced at 9.5-m intervals would only allow this to break the accumulation rates into roughly 4-m.y. increments, if we aim for an uncertainty better than ±20%.

The second uncertainty, of course, is the age of the datums. This uncertainty would be as large as the above example, were the datum ages determined within limits of about 0.5 m.y. Our aim was to use a prime set of datums, distributed less than 2 m.y. apart, and to determine these datums in all sites to within one section (1.5 m) or better.

Sedimentation rates (m/m.y.) may be estimated from age-vs.-depth plots, either by drawing best-fit lines through all the data over successive depth intervals, or by drawing straight-line segments (uniform sedimentation rate) between selected datums. For best comparison among sites, and to make optimum use of the most precisely determined datums, we have chosen the second solution. Inspection of the distribution of other datums about the lines suggests that it might be difficult to rigorously justify one approach vs. another, especially given the difficulty of evaluating the uncertainties in the accuracy of each datum. Plots of sedimentation rate vs. age must be evaluated in the light of the distribution of data points in the age-vs.-depth plots, which give a better impression of the evidence for or against rapid changes in sedimentation rate, because the method we used tends to exaggerate the suddenness of the changes. All sedimentation rates were calculated using mid-points in the observed depth uncertainty range. Note also that we show only uncertainties in depth in our sedimentation rate graphs. In reality, each datum event has an age uncertainty that may vary from a few thousand years to a few hundred thousand years.

Mass accumulation rates ($g/cm^2/1000$ yr) are calculated from linear sedimentation rates and so-called dry bulk density (gram dry sediment per wet volume). Given the difficulty in attaining a better than ±20% accuracy in linear sedimentation rate, uncertainties in density are a minor factor (although, strictly speaking, we should use density in situ because the drill string measures thickness in situ). We have used mean values for the appropriate intervals. Mass accumulation rates of calcium carbonate are first expressed in the same way (i.e., using mean values). Higher frequency variations in the percentage of carbonate obviously imply that higher frequency variations in the accumulations of either carbonates or noncarbonates are superimposed on relatively stable, long-term accumulation rates.

COMPOSITE DEPTHS

Composite Section Development

The recovery of sections having documented continuity over APC-cored intervals of the sedimentary sequence was crucial to the paleoceanographic objectives of Leg 154. Drilling of multiple APC holes at each site that are offset in depth has traditionally helped to

Table 3. Age estimates of planktonic foraminifer datum events.

Event	Zone (base)	Age (Ma)	Reference
T *Globorotalia tosaensis*		0.6	1
B *Pulleniatina finalis*		1.4	1
T *Globigerinoides fistulosus*		1.7	1
Pleistocene/Pliocene boundary		1.77	
T *Globigerina apertura*		1.9	2
T *Globigerinoides extremus*		1.9	1
B *Globorotalia truncatulinoides*	N22	2.0	2
T *Globorotalia exilis*		2.2	2
T *Globorotalia miocenica*		2.3	1
Reappearance of *Pulleniatina* (Atlantic)		2.3	1
T *Globigerina woodi*		2.3	2
T *Globigerina decoraperta*		2.6	2
T *Globorotalia pertenuis*		2.6	1
T *Dentoglobigerina altispira*		3.0	2
T *Globorotalia multicamerata*		3.0	1
T *Globorotalia conomiozea*		3.1	1
B *Globorotalia inflata*		3.1	1
T *Sphaeroidinellopsis seminulina*		3.1	2
B *Globorotalia tosaensis*	N21	3.2	2
B *Globigerinoides fistulosus*		3.2	2
B *Globorotalia crassula*		3.2	1
B *Globorotalia pertenuis*		3.5	1
T *Pulleniatina* (Atlantic)		3.5	1
B *Globorotalia miocenica*	N20	3.6	1
T *Globorotalia margaritae*		3.6	1
B *Globigerina rubescens*		3.6	2
Δ *Pulleniatina* (S to D coiling change)		4.0	2
T *Globigerina nepenthes*		4.3	2
T *Globorotalia plesiotumida*		4.4	2
B *Globorotalia crassaformis* s.l		4.7	1
B *Globorotalia puncticulata*		4.8	1
T *Globorotalia cibaoensis*		5.0	2
T *Neogloboquadrina acostaensis*		5.1	2
Pliocene/Miocene boundary		5.38	
T *Globorotalia juanai*		5.4	2
T *Globoquadrina baroemoensis*		5.4	2
B *Sphaeroidinella dehiscens* s.s.	N19	5.6	1
T *Globoquadrina dehiscens*		5.6	2
B *Globorotalia margaritae*		5.7	3
B *Globorotalia tumida*	N18	5.9	2
T *Globorotalia lenguaensis*		5.9	2
B *Globorotalia margaritae*		6.2	2
B Dextral menardine Globorotaliids		6.6	1
Δ *Neogloboquadrina acostaensis* (D to S)		6.7	1
B *Globorotalia conomiozea*		6.7	1
T Sinistral menardine Globorotaliids		7.2	1
B *Globorotalia cibaoensis*		7.7	2
B *Globorotalia juanai*		8.0	2
B *Candeina nitida*		8.0	2
B *Globigerinoides extremus*		8.0	2
B *Globorotalia plesiotumida*	N17	8.2	2
B *Neogloboquadrina acostaensis*	N16	10.0	2
T *Paragloborotalia mayeri*	N15	10.3	2
B *Globigerina apertura*		10.8	2
T *Globorotalia praemenardii*		10.7	2
B *Globigerina nepenthes*	N14	10.8	2
B *Globigerina decoraperta*		11.2	2
T *Fohsella fohsi* s.l.	N13	11.8	2
B *Globorotalia lenguaensis*		12.3	2
B *Fohsella fohsi robusta*		12.7	1
B *Fohsella fohsi* s.l.	N12	13.5	2
T *Globorotalia birnageae*		13.6	2
T *Globorotalia praescitula*		13.8	2
B *Fohsella "praefohsi"*	N11	14.0	2
T *Globorotalia archeomenardii*		14.2	2
T *Fohsella peripheroronda*		14.6	1
B *Fohsella peripheroacuta*	N10	14.7	2
B *Globorotalia praemenardii*		14.9	2
B *Orbulina* spp.	N9	15.1	1
B *Globorotalia archeomenardii*		15.5	2
B *Pulleniatina circularis*		16.0	1
B *Pulleniatina glomerosa*		16.1	1
T *Globigerinoides altiapertura*		16.2	2
B *Praeorbulina sicana*	N8	16.4	1
B *Globorotalia miozea*		16.6	1
T *Globorotalia zealandica*		16.6	1
T *Catapsydrax dissimilis*	N7	17.3	1
B *Globigerinatella insueta*	N6	18.7	1
B *Globorotalia praescitula*		19.1	2
T *Globoquadrina binaiensis*		19.1	2
T *Paragloborotalia kugleri*	N5	21.6	1
B *Globoquadrina binaiensis*		22.1	2
B *Globorotalia birnageae*		22.17	2
B *Globoquadrina dehiscens*		23.3	2
T *Globigerina angulisuturalis*		23.3	1
T *Globorotalia pseudokugleri*		23.3	1
B *Paragloborotalia kugleri*	N4	23.7	1
B *Globigerina euaperta*		23.7	3
Miocene/Oligocene boundary		23.8	
B *"Gs." primordius* (common)		24.5	4
T *Tenuitella gemma*		24.5	4
B *Paragloborotalia pseudokugleri*		26.3	4
B *Globigerinoides primordius*		26.7	4
T *Globigerina labiacrassata*		27.1	4
T *Paragloborotalia opima*	P22	27.1	4
T *Ch. cubensis* (common)	P21b	28.5	4
B *Globigerinita boweni*		28.5	4
B *"Globigerina" angulisuturalis*	P21a	29.7	4
B *Tenuitellinata juvenilis*		29.9	4
T *Subbotina angiporoides*		30.1	4
T *Turborotalia ampliapertura*	P20	30.3	4
B *Paragloborotalia opima*		30.6	4
T *Pseudohastigerina* spp.	P19	32.5	4
Oligocene/Eocene boundary		33.8	
T *Hantkenina* spp.		33.8	4
T *Turborotalia cerroazulensis* s.l.	P18	33.9	4
T *Cribrohantkenina inflata*	P17	34.0	4
T *Globigerinatheka index*		34.2	4
B *Turborotalia cunialensis*		35.1	4
T *Turborotalia pomeroli*		35.2	4
T *Globigerinatheka semiinvoluta*		35.2	4
B *Cribrohantkenina inflata*	P16	35.4	4
T *Subbotina linaperta*		37.5	4
T *Morozovella spinulosa*		38.1	4
B *Globigerinatheka semiinvoluta*	P15	38.8	4
T *Planorotalites* spp.		39.0	4
T *Acarinina primitiva*		39.7	4
T *Subbotina frontosa*		39.9	4
T *Orbulinoides beckmanni*	P14	40.2	4
B *Orbulinoides beckmanni*	P13	40.6	4
T *Acarinina bullbrooki*		40.6	4
B *Turborotalia pomeroli*		42.7	4
B *Globigerinatheka index*		43.2	4
B *Morozovella lehneri*		43.6	4
T *Morozovella aragonensis*	P12	43.7	4
B *Globigerinatheka kugleri*	P11	45.8	4
B *Subbotina possagnoensis*		45.8	4
B *Hantkenina nuttalli*	P10	49.0	4
B *Planorotalites palmerae*	P9	50.3	4
T *Morozovella formosa*	P8	50.8	4
B *Morozovella aragonensis*	P7	52.0	4
T *Morozovella marginodentata*		52.8	4
T *Morozovella lensiformis*		52.8	4
B *Morozovella formosa*	P6b	53.2	4
B *Morozovella lensiformis*		53.3	4
T *Morozovella aequa*		53.3	4
Eocene/Paleocene boundary		53.4	
T *Morozovella velascoensis*	P6a	53.4	4
T *Morozovella acuta*		53.4	4
B *Morozovella gracilis*		54.0	4
B *"Morozovella" broedermanni*		54.0	4
B *Morozovella acuta*		54.0	4
B *Morozovella marginodentata*		54.0	4
B *Globonomalina australiformis*		55.1	4
T *Globanomalina pseudomenardii*	P5	56.1	4
B *Morozovella subbotinae*		56.5	4
T *Acarinina acarinata*		57.0	4
T *Acarinina mckannai*		57.0	4
B *Acarinina soldadoensis*	P4c	56.7	4
B *Acarinina coalingensis*		56.7	4
B *Morozovella aequa*		56.7	4
T *Acarinina subsphaerica*	P4b	57.7	4
B *Acarinina mckannai*		58.1	4
B *Globanomalina pseudomenardii*	P4a	58.4	4
B *Acarinina subsphaerica*		58.6	4
B *Acarinina acarinata*		58.6	4
T *Parasubbotina variola*		58.7	4
T *Parasubbotina varianta*		58.7	4
B *"Morozovella" albeari*	P3b	60.2	4
B *Morozovella velascoensis*		60.2	4
B *Morozovella praepentacamerata*		60.3	4
B *Morozovella conicotruncata*		60.3	4
B *Morozovella angulata*	P3a	60.5	4
B *"Morozovella" pusilla*		61.4	4
B *Praemurica praecursoria*	P2	61.7	4
B *Praemurica praeangulata*		61.7	4
B *Globanomalina imitata*		62.1	4
B *Globanomlaina compressa*	P1c	63.5	4
B *Praemurica inconstans*		63.5	4
B *Parasubbotina varianta*		64.1	4
B *Subbotina triloculinoides*	P1b	65.3	4
T *Parvularugoglobigerina eugubina*	P1a	65.9	4
B *Parasubbotina pseudobulloides*		65.9	4
B *Parvularugoglobigerina eugubina*	Pa	66.0	4
T *Globotruncana* spp.	P0	66.1	4

Note: T = top, and B = bottom. S = sinistral, and D = dextral. References are as follows: 1 = Berggren et al. (1985a, 1985b), 2 = Chaisson and Leckie (1993), 3 = Berggren et al. (1985c), and 4 = Berggren et al. (in press).

ensure that intervals of no recovery in a single APC hole were recovered in an adjacent hole. During Leg 154, as with previous ODP legs, the continuity of recovery was confirmed by development of composite depth sections at the multiple-cored sites. The methodology used for composite section development during Leg 154 is explained in this section. The methods are similar to those used to construct composite depth sections during Leg 138 (Hagelberg et al., 1992).

At each site, high-resolution (3- to 10-cm interval) measurements of magnetic susceptibility, GRAPE wet bulk density, natural gamma emissions, and *P*-wave velocity were made on the MST soon after the cores were retrieved. These measurements were entered into the shipboard database. In addition, measurements of visible percentages of color reflectance were made at 5-cm resolution on the split cores (see "Lithostratigraphy" section, this chapter). Using magnetic susceptibility and color reflectance as the two primary lithologic parameters, as additional APC holes were drilled, the measurements from each hole were visually and quantitatively compared to determine if coring offsets were maintained between holes. Correlation of events present in multiple holes provided verification of the extent of recovery of the sedimentary sequence. Integration of at least two different physical properties (generally magnetic susceptibility and reflectance) allowed hole-to-hole correlations to be made with greater confidence than would be possible with only a single parameter.

Hole-to-hole correlations were made using interactive software developed specifically for this task. We used a prototype software package that was developed at Lamont Doherty Earth Observatory and patterned after the Leg 138 core correlation software. Corresponding features in the data from cores in adjacent holes were aligned using both graphical and quantitative cross-correlations. Correlative features were aligned by adjusting the ODP coring depths in meters below seafloor (mbsf) on a core-by-core basis. No depth adjustments were made within a core. The results from several lithologic parameters were integrated to resolve discrepancies. The resulting adjusted depth scale is the meters composite depth (mcd) scale. For each core at each site, the depth adjustment required to convert from mbsf to mcd is given in tabular form in the site chapter.

In general, the offsets applied arise from two sources. First, there are random uncertainties, arising primarily from ship motion, in the position of the drill bit at the moment the APC is "shot." Second, various poorly understood mechanisms (including rebound following core recovery and core expansion associated with mechanical distortion) ensure that the composite section is longer than the section in situ, typically by about 10%.

We sometimes observed that there is a systematic offset for the cores in a particular hole. This arises because the depth (mbsf) for every core in the hole is based on the position of the mud line recovered in the first core, which is subject to the same random variability as the depth of subsequent cores.

Figure 8 illustrates the need for hole-to-hole correlation and the mcd scale. In Figure 8A, magnetic susceptibility records from three holes at Site 927 are given on the mbsf depth scale. In Figure 8B, the same records are given after depth scale adjustment. After adjusting the depth scale so that features common to cores in all holes are aligned, a coring gap is indicated, for example, between Cores 154-927A-3H and -4H.

The correlation process was iterative. Records of a single physical parameter were moved along a depth scale core by core as correlations between the two holes were made. Although core distortion within a given core was in some cases significant, the core depths were only adjusted by a single constant for each core. The amount of adjustment necessary to optimize the correlation among multiple holes was retained for each core in each hole. As discussed below, depth adjustments for individual cores were also constrained so that a single spliced record could be sampled from the aligned cores without any additional depth scale changes. The same comparison was repeated for the other lithologic parameters to check the core adjustments. Where the amount of offset necessary to align features was ambiguous or uncertain for both lithologic parameters, or where multiple hole data was unavailable, no depth adjustment for that particular core was made. In these cases, the total amount of offset between mbsf and mcd is equal to the cumulative offsets from the overlying cores. When complete, confirmation of the composite depth section was provided by comparison with biostratigraphic data from multiple holes.

The composite depth section for each site is presented in tabular format. A portion of the composite depth table for Site 927 is given as an example in Table 4. For each section in each core, the last two columns in Table 4 give the depth offset applied to the ODP sub-bottom depth and the composite depth (in mcd) at the top of the section, respectively. The offset column facilitates conversion of sample depths that are recorded in ODP sub-bottom depths (mbsf) to composite section depth (mcd). By adding the amount of offset listed in Column 5 to the mbsf of a measurement taken in a particular core, the equivalent in mcd is obtained. It is important to use the data in the composite depth table to obtain the depth mbsf or mcd for any sample, particularly because a significant proportion of core sections are less than 150 cm long.

After composite depth construction, a single spliced record representative of the multiple cored sedimentary sequence was assembled. Because the missing intervals between successive cores in the sedimentary sequence from any single hole could be identified, it was possible to patch in these missing intervals with data from adjacent holes. Prototype software developed specifically for this application was used to identify tie points for each splice. By identifying the intervals where features present in the multiple holes were most highly correlated, it was possible to construct a spliced record without the danger of mistakenly duplicating any individual features or cycles. Because there is considerable stretching and/or compression of many sections of core relative to the same sections in adjacent holes, the precise length of the splice depends on which intervals of core are selected to build it. In particular, the upper parts of APC cores were generally expanded relative to equivalent intervals located within the middle part of the core in adjacent holes, and the bases of cores were relatively compressed (Fig. 9). To facilitate the generation of a splice having the same set of depth offsets as the composite, the composite section was constructed so that cores were placed in exact alignment with splice tie points (within the sampling resolution of the susceptibility and reflectance measurements). In general, this alignment is slightly different than the alignment that would give the highest overall hole-to-hole correlation, and thus sometimes gives the visual impression that core alignment is not perfect (Fig. 9). Further adjustments to the composite depth section on a within-core basis will be required to align all features exactly.

An example of a spliced magnetic susceptibility record from Site 927 is given in Figure 10. Figure 10A shows the spliced magnetic susceptibility record, and Figure 10B shows the composite hole data used to construct the splice. Tables that give the tie points for construction of the spliced record are given in each site chapter. A significant advantage of the spliced record is that it provides a single representative record of a lithologic parameter (i.e., susceptibility, color reflectance, or natural gamma) for a given site. This single record is ideally suited to serving as a sampling scheme for high-resolution paleoceanographic studies.

PALEOMAGNETISM

General Considerations

The paleomagnetic remanence of virtually all of the sediments measured during Leg 154 proved to record only a coring-derived overprint; hence, we were unable to provide any useful magnetostratigraphic age control. The brief discussions of paleomagnetism in the following site chapters summarize these negative magnetostrati-

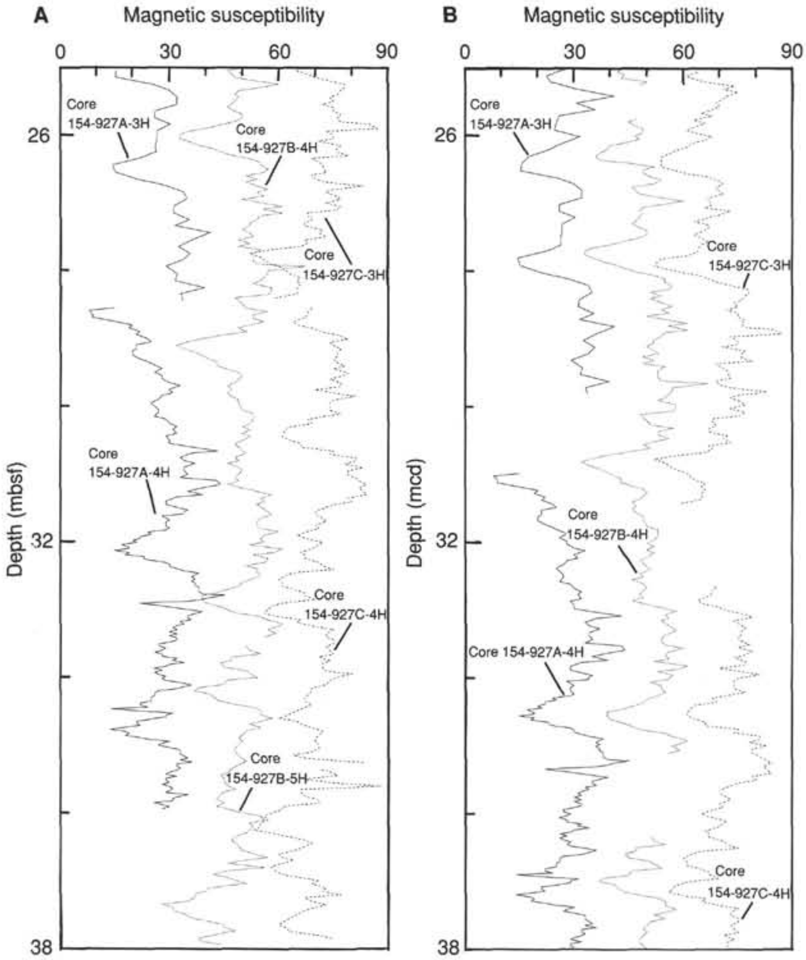

Figure 8. Portions of the magnetic susceptibility records from Site 927. **A.** Cores 154-927A-3H and -4H, 154-927B-4H and -5H, and 154-927C-3H and -4H on mbsf depth scale. Data from each hole are offset for clarity. Solid line = Hole 927A, dotted line = Hole 927B, and dashed line = Hole 927C. **B.** The same cores on the mcd depth scale. The composite depth section has the advantage that features common to all holes are in relative alignment.

graphic results and describe what we were able to learn of the nature of the pervasive remagnetization.

The more significant data collected during the leg were low-field magnetic susceptibilities. These data, along with reflectance measurements, provided the primary means for inter-hole and inter-site correlation (see "Composite Depths" section, this chapter).

Magnetic Polarity Reversal Time Scale

The lack of magnetostratigraphic results removes the requirement to adopt a particular nomenclature in discussing polarity reversal boundaries. Nevertheless, it is important to note that the age estimates for most of the biostratigraphic age controls used throughout the leg depend on magnetostratigraphies obtained elsewhere. Hence, the absolute ages assigned to these various biostratigraphic datums (see "Biostratigraphy" section, this chapter) will indeed depend on the particulars of the magnetic polarity time scale that is accepted. For this purpose, we have adopted a magnetic polarity time scale that is a composite of four previous time scales: Shackleton et al.'s (1990) astronomically tuned time scale for the interval between 0 and 2.6 Ma; Hilgen's (1991a, 1991b) astronomically tuned time scale for the interval between 2.6 and 5.23 Ma; Shackleton et al.'s (1994, table 17) time scale (partially astronomically tuned) for the interval between 5.23 and 14.8 Ma; and finally Cande and Kent's (1992) seafloor-spreading-based time scale for ages older than 14.8 Ma. These four separate time scales are compatible and should not introduce artificial discontinuities in calculated sedimentation rates where they have been joined. Absolute ages that make up the Leg 154 magnetic polarity time scale are summarized in Table 5.

Laboratory Facilities

The paleomagnetic laboratory is equipped with two magnetometers: a pass-through cryogenic superconducting rock magnetometer manufactured by 2-G Enterprises (Model 760R) and a Molspin spinner magnetometer. The sensing coils in the cryogenic magnetometer measure magnetization over an interval of roughly 15 cm, the coils for each axis having slightly different response curves. The large volume of material sensed (~200–300 cm^3) gives the cryogenic system an excellent sensitivity despite the relatively high background noise aboard the ship. In line with the pass-through cryogenic magnetometer is an alternating field (AF) demagnetizer, capable of alternating fields up to 35 mT (2-G Model 2G600).

The magnetic susceptibility of unsplit sections of core was measured with Bartington Instruments Model MS1 susceptibility meter adapted with a MS1/CX 80-mm whole-core sensor loop running at 0.465 kHz. The full width of the impulse response peak (at half maximum) is less than 5 cm. The susceptibility loop is mounted with the other physical properties sensors (GRAPE, natural gamma, and *P*-wave) on the MST.

Stepwise demagnetization of single samples was normally achieved with a Schonstedt model GSD-1 AF demagnetizer, which is capable of demagnetizing discrete specimens to 100 mT. We also performed thermal demagnetization on a small number of samples using the Schonstedt model TSD-1 thermal demagnetizer.

Ancillary laboratory equipment available during Leg 154 included a Kappabridge KLY-2 susceptibility bridge, which we used for most measurements of single samples. We also used the DTECH magnetizer to impart anhysteretic remanent magnetizations and the ASC impulse

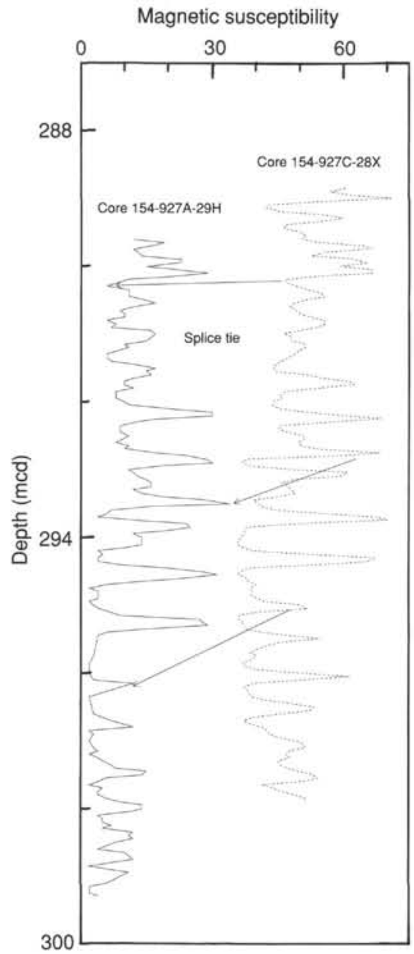

Figure 9. Alignment of Cores 154-927A-29H and 154-927C-28X on the composite depth scale illustrates the expansion and/or compression of relative features between holes, which makes exact alignment of all features on a core-by-core basis impossible. The data shown are magnetic susceptibility. For the purpose of constructing a splice, features corresponding to between-hole tie points were aligned exactly on the composite depth scale, leaving the remainder of the core slightly misaligned.

magnetizer (Model 1M-10), which is capable of generating fields up to 1.3 tesla (T), to produce isothermal remanent magnetizations.

Paleomagnetic Measurements

We made all paleomagnetic measurements using the cryogenic magnetometer. The bulk of these measurements were taken on archive half sections. However, we also used the cryogenic system to measure the discrete samples. For rapid measurement with blanket demagnetization treatment, we used the magnetometer as a pass-through system: we placed discrete samples at 20-cm intervals in the normal boat and used the standard ODP PC software. For more careful progressive demagnetization of discrete samples, we used the Schonstedt GSD-1 demagnetizer and measured the samples in four positions using an improvised sample holder and Macintosh-based data acquisition software.

In general, we performed pass-through paleomagnetic measurements on the archive halves of the 1.5-m core sections for all APC cores taken for at least one hole at each site. We routinely measured the natural remanent magnetization after 20-mT AF demagnetization using a 10-cm measurement interval.

The ODP core orientation convention designates the *x*-axis as the horizontal (in situ) axis radiating from the center of the core through the space between a double line scribed lengthwise on the working half of each core liner. All declinations reported are relative declinations measured with respect to this double line.

Data Archiving

Although it was rarely the case that we were able to measure a paleomagnetic remanence that could be reasonably ascribed to a primary component, we did archive a substantial amount of data that unfortunately reflects primarily a pervasive remagnetization. Although we generated various files of declination/inclination/intensity during the course of the leg, we chose to archive only the raw section files generated by the pass-through magnetometer rather than files of data processed more fully. This represents a compromise: it preserves the bulk of our observations in the ODP data archive, but at the same time signals that these data should not be used blithely for magnetostratigraphic interpretations.

Core Orientation

Orientation of the APC cores was conducted using the Tensor orientation tool. This tool consists of a 3-component fluxgate magnetometer and 3-component accelerometer rigidly attached to the core barrel, both of which enable it to record the drift of the hole and orientation of the double fiducial line on the plastic core liner. The Tensor tool was set to record at 30-s intervals, and these data were downloaded from the tool after several runs taking APC cores. In each case, all of the internal memory of the tool (1023 shots) was written to a file that was named to describe the hole as well as the beginning and ending cores (e.g., file 927B2328 contains data from Tensor tool shots taken for Cores 154-927B-23H to -28H). Core orientation was not attempted for the first two APCs at each site before the mud line was established. This prevented the possibility that the shock of a corer stroking out above the mud line might damage the orientation tool. Otherwise, core orientation was routinely taken for the APC cores. Notes on the orientation tool runs (start time, hold-off time, tool number, and bottom times) are archived in text file entitled "SHOTS.TXT."

The dearth of evidence for a primary magnetization recorded in the sediments prevented us from confirming that the Tensor tool was working reliably. Indeed, some evidence exists that the Tensor results may be contaminated by stray fields of the bottom-hole assembly (BHA): orientation data recorded during stable intervals when the core was at the bottom of the hole indicate a magnetic field of approximately 44,000 nT at 50° inclination: this is considerably different from the ambient field in this region, which is approximately 29,000 nT at 12° inclination. Nevertheless, the stray fields may be vertical, in which case the Tensor "MTF" angle would be valid. In this case, true declination could be derived from relative declination by adding the Tensor MTF angle and subtracting the local magnetic variation (which is about 20°W here).

Low-field Susceptibility

Whole-core volume magnetic susceptibility was measured using the automated MST in conjunction with gamma-ray-attenuation, natural gamma, and *P*-wave sensors. Measurements were performed on whole-round sections with the Bartington MS1 meter using either the high-sensitivity range (0.1) or low-sensitivity (1.0) ranges at varying intervals, depending on the time available for these on-board measurements and on the strength of the susceptibility signal. All measurements were taken in the "cgs" mode. Susceptibility data were archived in raw instrument units that require a single multiplicative factor of 7.7×10^{-6} to convert to volume-normalized SI units. However, this conversion assumes that the core liner was completely filled with sediment, an assumption that is not generally true for XCB- and rotary-cored intervals. We checked the calibration factor by compar-

Table 4. Composite depth section, Site 927.

Core and section	Section length (cm)	Depth (mbsf)	Offset (m)	Composite depth (mcd)
155-927A-				
1H-1	150	0	0.31	0.31
1H-2	150	1.5	0.31	1.81
1H-3	150	3	0.31	3.31
1H-4	150	4.5	0.31	4.81
1H-5	150	6	0.31	6.31
1H-6	131	7.5	0.31	7.81
1H-CC	15	8.81	0.31	9.12
2H-1	150	9.5	0.91	10.41
2H-2	150	11	0.91	11.91
2H-3	150	12.5	0.91	13.41
2H-4	150	14	0.91	14.91
2H-5	150	15.5	0.91	16.41
2H-6	150	17	0.91	17.91
2H-7	46	18.5	0.91	19.41
2H-CC	14	18.96	0.91	19.87
155-927B-				
1H-1	150	0	0	0
1H-2	150	1.5	0	1.5
1H-3	100	3	0	3
1H-4	57	4	0	4
1H-CC	18	4.57	0	4.57
2H-1	150	5	0.41	5.41
2H-2	150	6.5	0.41	6.91
2H-3	150	8	0.41	8.41
2H-4	150	9.5	0.41	9.91
2H-5	150	11	0.41	11.41
2H-6	150	12.5	0.41	12.91
2H-7	51	14	0.41	14.41
2H-CC	15	14.51	0.41	14.92
154-927C-				
1H-1	150	0	0.5	0.5
1H-2	150	1.5	0.5	2
1H-3	150	3	0.5	3.5
1H-4	150	4.5	0.5	5
1H-5	150	6	0.5	6.5
1H-6	142	7.5	0.5	8
1H-CC	31	8.92	0.5	9.42
2H-1	150	9.5	3.41	12.91
2H-2	150	11	3.41	14.41
2H-3	150	12.5	3.41	15.91
2H-4	150	14	3.41	17.41
2H-5	150	15.5	3.41	18.91
2H-6	150	17	3.41	20.41
2H-7	50	18.5	3.41	21.91
2H-CC	28	19	3.41	22.41
3H-1	150	19	3.02	22.02
3H-2	150	20.5	3.02	23.52
3H-3	150	22	3.02	25.02
3H-4	150	23.5	3.02	26.52
3H-5	150	25	3.02	28.02
3H-6	150	26.5	3.02	29.52
3H-7	42	28	3.02	31.02
3H-CC	28	28.42	3.02	31.44

ing MST susceptibility values over several intervals against Kappa-bridge measurements of discrete samples.

GEOCHEMISTRY

Interstitial-water Sampling and Chemistry

Shipboard interstitial-water analyses were performed on 5- to 15-cm-long, whole-round sections that were cut immediately after the core arrived on deck. Samples were usually taken from the bottom of section three of each of the first six cores, and from each third core thereafter. A high-resolution suite of 5-cm-long, whole-round samples was taken at ~1.5-m intervals from the top 50 m of Holes 925E and 929A. Interstitial waters were collected by applying pressure to the sediment using a titanium and stainless steel squeezer (Manheim and Sayles, 1974). Before squeezing, each whole-round surface was carefully scraped with a spatula to remove potentially contaminated exteriors. Each whole-round section was then placed into a titanium cylinder atop a Whatman No. 1 filter previously rinsed in high purity water to remove processing acids. A second filter paper and a stainless steel piston were placed on top of the sample in the cylinder and up to 40,000-lb pressure (approximately 4150 psi) was applied with a hydraulic press.

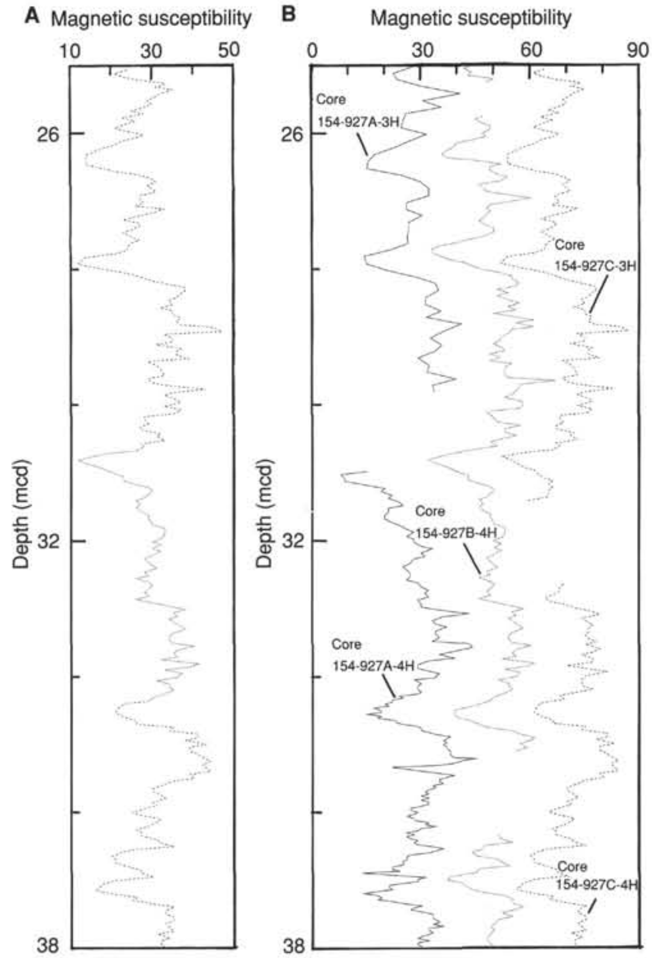

Figure 10. **A.** Portion of spliced magnetic susceptibility record from Site 927. **B.** Composite core data from the three Site 927 holes. Data from Holes 927B and 927C are offset for clarity.

Interstitial water was expressed into a plastic syringe attached to the bottom of the assembly and filtered through a 0.45-μm Gelman polysulfone disposable filter. Samples were stored in plastic vials pending analysis. Aliquots for future shore-based analyses were placed in acid-washed plastic tubes and glass ampoules and heat-sealed.

Interstitial-water samples were routinely analyzed, using the analytical techniques described by Gieskes et al. (1991), for salinity as total dissolved solids (g/kg) with a Goldberg optical hand-held refractometer (Reichart); for pH and alkalinity by Gran titration with a Brinkmann pH electrode and a Metrohm autotitrator; for dissolved chloride, calcium ("routine method"), and magnesium ("routine method") concentrations by titration; and for silica, phosphate (Sites 925 and 929 only), and ammonium by spectrophotometric methods with a Milton Roy Spectronic 301 spectrophotometer. International Association of Physical Sciences Organizations (IAPSO) standard seawater was used for calibrating most techniques. The reproducibility of these analyses, expressed as 1 σ standard deviations of means of multiple determinations of IAPSO standard seawater or of an internal standard, are alkalinity = <1.5%, chloride = 0.4%, calcium = <1%, magnesium = 0.5%, and silica, phosphate, and ammonium = 4%–5%. At all sites, a minor correction to the calcium and magnesium results was applied to account for strontium in the samples. In the few cases where strontium was not determined for a sample, no correction was applied. At Site 925, the initial chloride determinations were of variable quality because of the formation of precipitates within the tip of the autotitrator. In addition, repeat titrations attempted later with a

Table 5. Ages accepted for the magnetic polarity time scale.

Boundary	Age	Reference
C1n "Brunhes" (o)	0.78	SBP90
C1r.1n "Jaramillo" (t)	0.99	SBP90
C1r.1n "Jaramillo" (o)	1.07	SBP90
C2n "Olduvai" (t)	1.77	SBP90
C2n "Olduvai" (o)	1.95	SBP90
C2An.1n "Gauss" (t)	2.60	SBP90/H91
C2An.1r "Kaena" (t)	3.04	H91
C2An.1r "Kaena" (o)	3.11	H91
C2An.2r "Mammoth" (t)	3.22	H91
C2An.2r "Mammoth" (o)	3.33	H91
C2Ar "Gilbert" (t)	3.58	H91
C3n.1n "Cochiti" (t)	4.18	H91
C3n.1n "Cochiti" (o)	4.29	H91
C3n.2n "Nunivak" (t)	4.48	H91
C3n.2n "Nunivak" (o)	4.62	H91
C3n.3n "Sidufjall" (t)	4.80	H91
C3n.3n "Sidufjall" (o)	4.89	H91
C3n.4n "Thvera" (t)	4.98	H91
C3n.4n "Thvera" (o)	5.23	H91/SCHPS94
C3A.n1 (t)	5.875	SCHPS94
C3A.n1 (o)	6.122	SCHPS94
C3A.n2 (t)	6.256	SCHPS94
C3A.n2 (o)	6.555	SCHPS94
C3Bn (t)	6.919	SCHPS94
C3Bn (o)	7.072	SCHPS94
C4n.1n (t)	7.406	SCHPS94
C4n.1n (o)	7.533	SCHPS94
C4n.2n (t)	7.618	SCHPS94
C4n.2n (o)	8.027	SCHPS94
C4r.1n (t)	8.174	SCHPS94
C4r.1n (o)	8.205	SCHPS94
C4An (t)	8.631	SCHPS94
C4An (o)	8.945	SCHPS94
C4Ar.1n (t)	9.142	SCHPS94
C4Ar.1n (o)	9.218	SCHPS94
C4Ar.2n (t)	9.482	SCHPS94
C4Ar.2n (o)	9.543	SCHPS94
C5n.1n (t)	9.639	SCHPS94
C5n.2n (o)	10.839	SCHPS94
C5r.1n (t)	10.943	SCHPS94
C5r.1n (o)	10.991	SCHPS94
C5r.2n (t)	11.373	SCHPS94
C5r.2n (o)	11.428	SCHPS94
C5An.1n (t)	11.841	SCHPS94
C5An.1n (o)	11.988	SCHPS94
C5An.2n (t)	12.096	SCHPS94
C5An.2n (o)	12.320	SCHPS94
C5Ar.1n (t)	12.605	SCHPS94
C5Ar.1n (o)	12.637	SCHPS94
C5Ar.2n (t)	12.705	SCHPS94
C5Ar.2n (o)	12.752	SCHPS94
C5AAn (t)	12.929	SCHPS94
C5AAn (o)	13.083	SCHPS94
C5ABn (t)	13.252	SCHPS94
C5ABn (o)	13.466	SCHPS94
C5ACn (t)	13.666	SCHPS94
C5ACn (o)	14.053	SCHPS94
C5ADn (t)	14.159	SCHPS94
C5ADn (o)	14.607	SCHPS94
C5Bn.1n (t)	14.800	SCHPS94/CK92
C5Bn.1n (o)	14.890	CK92
C5Bn.2n (t)	15.038	CK92
C5Bn.2n (o)	15.162	CK92
C5Cn.1n (t)	16.035	CK92
C5Cn.1n (o)	16.318	CK92
C5Cn.2n (t)	16.352	CK92
C5Cn.2n (o)	16.515	CK92
C5Cn.3n (t)	16.583	CK92
C5Cn.3n (o)	16.755	CK92
C5Dn (t)	17.310	CK92
C5Dn (o)	17.650	CK92
C5En (t)	18.317	CK92
C5En (o)	18.817	CK92
C6n (t)	19.083	CK92
C6n (o)	20.162	CK92
C6An.1n (t)	20.546	CK92
C6An.1n (o)	20.752	CK92
C6An.2n (t)	21.021	CK92
C6An.2n (o)	21.343	CK92
C6AAn (t)	21.787	CK92
C6AAn (o)	21.877	CK92
C6AAr.1n (t)	22.166	CK92
C6AAr.1n (o)	22.263	CK92
C6AAr.2n (t)	22.471	CK92
C6AAr.2n (o)	22.505	CK92
C6Bn.1n (t)	22.599	CK92
C6Bn.1n (o)	22.760	CK92
C6Bn.2n (t)	22.814	CK92
C6Bn.2n (o)	23.076	CK92
C6Cn.1n (t)	23.357	CK92
C6Cn.1n (o)	23.537	CK92
C6Cn.2n (t)	23.678	CK92
C6Cn.2n (o)	23.800	CK92
C6Cn.3n (t)	23.997	CK92
C6Cn.3n (o)	24.115	CK92
C7n.1n (t)	24.722	CK92
C7n.1n (o)	24.772	CK92
C7n.2n (t)	24.826	CK92
C7n.2n (o)	25.171	CK92
C7An (t)	25.482	CK92
C7An (o)	25.633	CK92
C8n.1n (t)	25.807	CK92
C8n.1n (o)	25.934	CK92
C8n.2n (t)	25.974	CK92
C8n.2n (o)	26.533	CK92
C9n (t)	27.004	CK92
C9n (o)	27.946	CK92
C10n.1n (t)	28.255	CK92
C10n.1n (o)	28.484	CK92
C10n.2n (t)	28.550	CK92
C10n.2n (o)	28.716	CK92
C11n.1n (t)	29.373	CK92
C11n.1n (o)	29.633	CK92
C11n.2n (t)	29.737	CK92
C11n.2n (o)	30.071	CK92
C12n (t)	30.452	CK92
C12n (o)	30.915	CK92
C13n (t)	33.050	CK92
C13n (o)	33.543	CK92
C15n (t)	34.669	CK92
C15n (o)	34.959	CK92
C16n.1n (t)	35.368	CK92
C16n.1n (o)	35.554	CK92
C16n.2n (t)	35.716	CK92
C16n.2n (o)	36.383	CK92
C17n.1n (t)	36.665	CK92
C17n.1n (o)	37.534	CK92
C17n.2n (t)	37.667	CK92
C17n.2n (o)	37.915	CK92
C17n.3n (t)	37.988	CK92
C17n.3n (o)	38.183	CK92
C18n.1n (t)	38.500	CK92
C18n.1n (o)	39.634	CK92
C18n.2n (t)	39.718	CK92
C18n.2n (o)	40.221	CK92
C19n (t)	41.353	CK92
C19n (o)	41.617	CK92
C20n (t)	42.629	CK92
C20n (o)	43.868	CK92
C21n (t)	46.284	CK92
C21n (o)	47.861	CK92
C22n (t)	48.947	CK92
C2n (o)	49.603	CK92
C23n.1n (t)	50.646	CK92
C23n.1n (o)	50.812	CK92
C23n.2n (t)	50.913	CK92
C23n.2n (o)	51.609	CK92
C24n.1n (t)	52.238	CK92
C24n.1n (o)	52.544	CK92
C24n.2n (t)	52.641	CK92
C24n.2n (o)	52.685	CK92
C24n.3n (t)	52.791	CK92
C24n.3n (o)	53.250	CK92
C25n (t)	55.981	CK92
C25n (o)	56.515	CK92
C26n (t)	57.800	CK92
C26n (o)	58.197	CK92
C27n (t)	61.555	CK92
C27n (o)	61.951	CK92
C28n (t)	63.303	CK92
C28n (o)	64.542	CK92
C29n (t)	64.911	CK92
C29n (o)	65.732	CK92
C30n (t)	66.601	CK92
C30n (o)	68.625	CK92
C31n (t)	68.745	CK92
C31n (o)	69.683	CK92
C32n.1n (t)	71.722	CK92
C32n.1n (o)	71.943	CK92
C32n.2n (t)	72.147	CK92
C32n.2n (o)	73.288	CK92
C32r.1n (t)	73.517	CK92
C32r.1n (o)	73.584	CK92
C33n (t)	73.781	CK92
C33n (o)	78.781	CK92
C34n (t)	83.000	CK92

Notes: (o) = onset, and (t) = termination. References are as follows: SBP90 = Shackleton et al. (1990); H91 = Hilgen (1991a, 1991b); SCHPS94 = Shackleton et al. (in press), table 17; and CK92 = Cande and Kent (1992).

new autotitrator appeared to show the effects of evaporation of samples, although at the next sites, there appeared to be no evaporation effect on IAPSO stored in the same sample vials. At all sites, sodium was determined using charge balance calculations where Σ(cation charge) = Σ(anion charge). Sodium calculations at Site 925 reflect the somewhat less reliable chloride data from that site.

Potassium and sulfate were determined by ion chromatography using the Dionex DX-100. The reproducibility of these analyses, expressed as 1 σ standard deviations of means of multiple determinations of IAPSO standard seawater, are potassium = <3% and sulfate = 4%. Calcium, magnesium, sodium, and chloride were also routinely determined using the ion chromatograph, but those results are not reported because titrations (calcium, magnesium, and chloride) and charge balance calculations (sodium) provided more accurate and precise results. For calcium, a 4%–8% relative error (1 σ standard deviation of repeat IAPSO determinations/published IAPSO concentration) of IAPSO standards was obtained with the ion chromatograph as opposed to <1% by titration. For magnesium, this error was 2%–5% with the ion chromatograph, which also compared unfavorably with the <0.5% relative error by titration. For both magnesium and calcium, downcore profiles are generally much smoother when determined by titration, a reflection of the smaller error inherent in that technique. The ion chromatograph results were a useful check on the general trends of calcium and magnesium. The ion chromatograph method is not optimized for the high concentrations of sodium and chloride that exist in the samples relative to the concentrations of the other constituents. Thus, for both chloride and sodium, the ion chromatograph results were unreliable, with highly exaggerated downcore fluctuations over an unreasonably large range of values. For example, at Site 926 sodium, as determined by ion chromatograph ranged from 453 to 509 mM, with the difference in concentration between adjacent samples (taken 30 m apart within the sediment column) up to 48 mM. Chloride determinations were similarly unreliable. We tried to develop a more precise method for chloride, using greater sample dilutions, but we had little success.

Strontium, lithium, iron (except Site 925), and manganese (Sites 925 and 929 only) concentrations were measured using flame spectrophotometric techniques with a Varian SpectrAA-20 atomic absorption unit. Lithium standards and some samples were determined on 1/5 diluted aliquots in nanopure water; more concentrated samples were diluted 1/10. Strontium standard concentrations were determined on 1/10 diluted aliquots, and sample concentrations were determined on 1/10, 1/20, 1/30, and 1/40 diluted aliquots, with increasing dilution as sample concentrations increased. Lithium was determined by emission using an air-acetylene flame, and strontium by atomic absorption using a nitrous oxide–acetylene flame with lanthanum chloride as an ionization suppressant. Iron samples were acidified immediately after squeezing with 100 µL of concentrated HCl added to each ~5 mL sample aliquot to prevent precipitation of iron hydroxides. The samples were analyzed without dilution. Manganese concentrations were determined on 1/5 diluted aliquots, with lanthanum chloride used as an ionization suppressant. Iron and manganese were determined by atomic absorption using an air-acetylene flame. Highly erratic iron results indicated that the pore waters had been contaminated during drilling operations, and we do not report dissolved iron concentrations in this volume. Standards for all flame spectrophotometric techniques were matched in matrix composition to the samples. The reproducibility of these techniques, expressed as 1 σ standard deviations of means of multiple determinations of IAPSO standard seawater or of a standard treated as samples, are strontium = <4%, lithium = <1%–2%, and manganese = 2%–3%.

Chemical data for interstitial waters are reported in molar units.

Carbon Geochemistry

The shipboard carbon geochemistry program for Leg 154 included (1) a real-time monitoring of the volatile hydrocarbons as required by safety considerations, (2) measurement of inorganic carbon concentration to determine the amount of carbonate in the sediments, and (3) elemental analysis of total nitrogen, carbon, and sulfur. The general procedures are described by Emeis and Kvenvolden (1986), with modifications noted for the headspace and total carbon analyses.

Hydrocarbon Gases

As required by safety considerations, concentrations of the light hydrocarbons methane (C_1), ethane (C_2), and propane (C_3) were monitored in the sediment cores at intervals of approximately 10 m. Only methane was identified at all sites. Headspace samples were obtained by removing a 5-cm^3 plug of sediment from the end of a core as it arrived on deck, using a No. 6 cork borer (Kvenvolden and McDonald, 1986). The sample was placed immediately in a 21-mL glass vial that was sealed with a septum and metal crimp and then heated to 70°C for at least 30 min. The gas driven off was drawn into a syringe and analyzed.

The gas samples were injected into a Hach-Carle AGC Series 100, Model 211 gas chromatograph equipped with a flame ionization detector and a 6-ft × ⅛-in. steel column packed with Porapak N:Q (80%/20%). The instrument has a detection limit for methane of 0.1 ppm. Details of this method and the complete configuration of the gas chromatograph are given in the "Explanatory Notes" chapter of Leg 112 (Suess, von Huene, et al., 1988).

Inorganic Carbon

Inorganic carbon was determined using a Coulometrics 5011 Carbon Dioxide Coulometer equipped with a System 140 carbonate carbon analyzer. Generally, three samples per core were analyzed. A known mass, ranging from 8 to 15 mg, of freeze-dried (dedicated carbonate samples) or oven-dried (physical properties samples) ground sediment was reacted in a 2N HCl solution. The liberated CO_2 was titrated in a monoethanolamine solution with a colorimetric indicator, while the change in light transmittance was monitored with a photo-detection cell. The percentage of carbonate was calculated from the inorganic carbon content, assuming that all carbonate occurs as calcium carbonate as follows:

$$CaCO_3 = \text{IC (inorganic carbon)} \times 8.33.$$

No corrections were made for possible contributions from siderite or dolomite. The precision of these analyses, expressed as 1 σ standard deviations of means of multiple determinations of a pure carbonate standard, was <1%.

Elemental Analysis

Total nitrogen, carbon, and sulfur of sediment samples were determined using an N.C.S. analyzer, Model NA 1500 from Carlo Erba Instruments. Mixtures of vanadium pentoxide (used at Sites 925, 926, and 927 only) and crushed, freeze-dried samples (~5 mg) were combusted in an oxygen atmosphere at 1000°C, converting organic and inorganic carbon to CO_2, sulfur to SO_2, and nitrogen to NO_2. The NO_2 was reduced to N_2 using copper. The gases were then separated by gas chromatography and measured with a thermal conductivity detector. The precision of these analyses, expressed as 1 σ standard deviations of means of multiple determinations of an estuarine sediment standard, is 2%–3%. Total organic carbon (TOC) was calculated as the difference between total carbon (TC) from the NCS and inorganic carbon (IC) from the Coulometer:

$$\text{TOC} = \text{TC} - \text{IC}.$$

PHYSICAL PROPERTIES

Introduction

General Objectives

The standard procedures for shipboard measurement of physical properties were slightly modified to serve a number of objectives unique to Leg 154. The principal objectives for the physical properties group follow from the science strategy of this expedition. They can be grouped as follows:

1. To provide high-resolution data for construction of a complete stratigraphic section;
2. To determine stress history of lithologic units for control on the mass accumulation rates, definition of erosional unconformities, and delineation of overconsolidated units as compared with diagenetically altered units; and
3. To determine heat flow on the Ceara Rise.

Standard shipboard measurements of physical properties include nondestructive, whole-core, MST measurements (*P*-wave velocity, magnetic susceptibility, GRAPE, and natural gamma), undrained shear strength, thermal conductivity, electrical resistivity, compressional-wave velocity, and index properties. Sampling frequency for discrete measurements was three per core when the MST data were of high quality. Over intervals in which the MST data were poor, the discrete measurement interval was increased to two per section. The MST sample frequency was one measurement every 1–3 cm for GRAPE, 3–10 cm for magnetic susceptibility, 10–15 cm for natural gamma, and 2 cm for the *P*-wave velocity. GRAPE and *P*-wave velocity were measured while the track was moving, and magnetic susceptibility and natural gamma while it was stationary. Note that the software controlling the MST allows the operator to specify the position of the first measurement and the sampling interval, but not the position of the last measurement. Thus, the last measurement of each section may be biased by an edge effect unless the operator entered a shorter length than the actual length of the section being measured.

Sampling Strategy

To accommodate the general objectives, the sampling program for physical properties was planned to fulfill several requirements:

1. To provide a complete record of properties of recovered core. Generally, sections were processed through the MST before subsampling for whole rounds. Discrete index samples were selected on the average of two per section when the MST was not run and three per core when the MST was run. Shear strength and resistivity were also measured at an interval of two per section or three per core at each site.
2. To cross-correlate and calibrate shipboard analyses. Samples were selected based on the MST results for calibration of the GRAPE and *P*-wave logger. Analyses of all physical properties were made on common sample intervals to avoid aliasing of data sets.
3. To calibrate downhole logs. Natural gamma, bulk density, porosity, acoustic velocity, and thermal conductivity from core samples are all valuable for core-log data integration.

Laboratory Measurements

Index Properties

Index properties (bulk density, grain density, water content, porosity, and dry density) were determined from measurements of wet and dry sediment mass and wet sediment volumes. Quality checks on these measurements were made by selective measurement of dry sample volumes. Samples of approximately 10 cm^3 were taken for determination of index properties. In addition, whole-core determination of bulk density was measured on cores that completely filled the liner using the GRAPE on the MST.

Sample mass was determined aboard ship to a precision of ±0.01 g using the Scitech electronic balance. The sample mass was counterbalanced by a known mass such that only mass differentials of less than 5 g usually were measured. Volumes were determined using either the Quantachrome Penta-Pycnometer, a helium-displacement pycnometer, or by sampling a constant volume of sediment from the core. The Quantachrome pycnometer measures volumes to an approximate precision of ±0.02 cm^3. Sample volumes were repeated until two consecutive measurements yielded volumes within 0.02 cm^3 of each other. A reference volume was run with each group of samples. The standard was rotated among the cells. Constant volumes were sampled using a syringe with a volume of 8.48 cm^3 for soft sediment. In hard sediment, cubes were cut using the double-bladed saw and individual sample dimensions were measured using the LVDT on the Hamilton Frame.

The tare beaker calibrations, which are used for discrete index property determinations using this pycnometer, were checked for mass and volume during the leg. This recalibration was conducted using the known density of the beakers and determining the mass of each with the Scitech balance. The ODP physical properties data base was updated with these corrected values.

Water Content

The determination of water content followed the methods of the American Society for Testing and Materials (ASTM) designation (D) 2216 (ASTM, 1989). As outlined in ASTM D2216, corrections are required for salt when measuring marine samples. All measurements were corrected for salt assuming a pore salinity of 35‰. In addition to the recommended water content calculation, the ratio of the pore fluid mass to the dry sediment mass (dry mass%) presented in ASTM D2216, a calculation of the ratio of pore fluid mass to total sample mass, was also reported (wet mass%). The equations for each water content calculation are as follows:

$$W_c \text{ (dry wt\%)} = (M_t - M_d)/(M_d - r_t) \tag{1}$$

$$W_c \text{ (wet wt\%)} = (M_t - M_d)/(1 - r)\, M_t, \tag{2}$$

where M_t = total mass (saturated), M_d = dry mass, and r = salinity.

Bulk Density

Bulk density (ρ) is the density of the total sample, including the pore fluid (i.e., $\rho = M_t/V_t$), where V_t is the total sample volume. Total mass (M_t) was measured using the electronic balance, and total volume was measured with the helium pycnometer or sampled as a constant volume. In high-porosity sediment, bulk density was calculated directly using $\rho = M_t/V_t$. A calculation check was performed on the bulk-density results using the specific gravity (G_s). Specific gravity was calculated using measured bulk density and water content as follows:

$$G_s = \rho/[\rho_{w-} W_c\,(r - \rho_w)], \tag{3}$$

where ρ_w = density of pore fluid, and W_c = water content reported as a decimal ratio of percentage dry mass.

Specific gravity was directly measured in the penta-pycnometer on selected samples from different lithologies. When the calculated specific gravity deviated from these known values for the measured lithologies or from the measured grain density, the bulk density reported was calculated from water content and grain density. The calculated bulk density values are used in the raw data tables as ρ_{calc} and were determined as follows:

$$\rho_{calc} = (1 + W_c)/\{1 + [W_c \times (\rho_{grain}/\rho_w)]\}) \times \rho_{grain}, \tag{4}$$

where W_c is the water content expressed as the ratio of pore-water mass to dry mass.

Porosity

Porosity was calculated using the following equation:

$$\eta = (W_c \times \rho)/[(1 + W_c) \times \rho_w], \tag{5}$$

where ρ, as used in the equation, is either the directly measured bulk density or ρ_{calc}, and W_c = water content reported as a decimal ratio of percent dry mass.

Grain Density

Grain density was determined directly on selected intervals from the dry mass (Scitech balance) and dry volume (pycnometer) measurements. Both mass and volume were corrected for salt as follows:

$$\rho_{grain} = (M_d - s)/[V_d - (s/\rho_{salt})], \quad (6)$$

where V_d = dry volume; s = mass of salt in the pore fluid, calculated from M_w/ρ_w; and ρ_{salt} = density of salt (2.257 g/cm^3).

Dry Density

Dry density is the ratio of the dry mass (M_d) to the total volume (V_t). Dry density was calculated using corrected water content and porosity for each measurement:

$$\rho_d = (\eta/W_c) \times \rho_w . \quad (7)$$

Multisensor Track (MST)

The MST incorporates the gamma-ray porosity evaluator (GRAPE), *P*-wave logger (PWL), magnetic susceptibility sensors, and natural gamma (NG). Individual unsplit core sections were placed horizontally on the MST, which moves the section through the four sets of sensors.

The GRAPE makes measurements of bulk density at 1-cm intervals by comparing the attenuation of gamma rays through the cores with attenuation through an aluminum standard (Boyce, 1976). The GRAPE data were most reliable in APC and undisturbed XCB and RCB cores. In XCB and RCB cores where the sediment does not fill the liner, the GRAPE measurements have no meaning in terms of density estimation but may be used in conjunction with discrete density measurements to provide an estimate of core diameter and hence to correct magnetic susceptibility and natural gamma measurements for the reduction in volume. The data reported here are corrected for the fact that in high-porosity sediment one cannot make the assumption that the sample is close to quartz in atomic number. In addition to the aluminum and air standard by which the GRAPE is calibrated, GRAPE was run when the water-filled *P*-wave standard was run as an additional check. The water standard measurement should result in an uncorrected density of 1.1 Mg/m^3 and a corrected density of 1.0 Mg/m^3. During most of Leg 154, high values of water density were routinely measured, indicative of one of several problems with GRAPE measurements identified during the leg. Initially, at Site 925, the procedure for calibrating the GRAPE using the standard proved inadequate and was modified. Drift problems, which were likely associated with the counting electronics, were identified during measurement at Sites 926, 927, and 928. The counting electronics were changed before beginning Site 928. At Site 928, an additional problem associated with electronic cross-talk between the *P*-wave logger and the GRAPE caused an offset in GRAPE counts. This offset likely caused the high-density measurements in the water standard.

The PWL transmits a 500-kHz compressional-wave pulse through the core at a repetition rate of 1 kHz. The transmitting and receiving transducers are aligned perpendicular to the core axis. A pair of displacement transducers monitors the separation between the compressional-wave transducers; variations in the outside diameter of the liner, therefore, do not degrade the accuracy of the velocities. Measurements are taken at 2-cm intervals. Only the APC and undisturbed XCB and RCB cores were measured. The velocity data are corrected to values in situ (see "Velocimetry" section, below).

Magnetic susceptibility was measured on all sections at 3- to 10-cm intervals using either the 0.1 or the 1.0 range on the Bartington meter with an 8-cm-diameter loop (refer to "Paleomagnetism" section [this chapter] for measurement details). The quality of these results degrades in XCB and RCB sections where the core is undersized and/or disturbed. However, used with care, the data are still useful for stratigraphic correlation.

Natural gamma radiation (NGR) was measured at 10- to 15-cm intervals in at least one hole at each site, both to provide a high-resolution record and for correlation with the downhole log. Background radiation was measured by using the water-filled core liner, which also serves to calibrate the *P*-wave logger, at least once per 12 hr. The background radiation values for each counting channel that were subtracted from subsequent measurements were based on 107 10-s counts with the water-filled core liner; they are as follows: 200–500 keV, 4.6 (0.86); 500–1100 keV, 2.1 (0.53); 1100–1590 keV, 0.66 (0.26); 1590–2000, 0.20 (0.14); 200–3000 keV, 0.35 (0.17); total = 7.9 (0.11) (the number in parentheses is the standard deviation; it is close to the theoretical number for 10-s counts given by Hoppie et al. [in press]). Corrections for sampling volume as proposed by Hoppie et al. (in press) were not made because of time constraints. Conversion of natural gamma from units of counts per second (cps) to gamma-ray American Petroleum Institute (API) units should be done following the methods of Hoppie et al. (in press) after correction for varying sample volume. In this volume, data are reported in cps.

Velocimetry

Compressional-wave (*P*-wave) velocity measurements were obtained using one of two different systems, depending on the degree of lithification of the sediment. In softer sediment, *P*-wave velocities were measured using a Dalhousie University/Bedford Institute of Oceanography digital sound velocimeter (DSV). Velocity calculation is based on the accurate measurement of the time for an acoustic signal to travel between a pair of piezoelectric transducers inserted in the split sediment cores. Two transducers separated by approximately 7 cm were used to measure the vertical (along the core axis) *P*-wave velocity. The transducers are firmly fixed at one end to a steel plate so that their separation will not change during velocity determinations. The transducers emit a 2-µs square wave at about 250 and 750 kHz. A dedicated microcomputer controls all functions of the velocimeter. The transmitted and received signals are digitized by a Nicolet 320 digital oscilloscope and transferred to the microcomputer for processing. The DSV software selects the first arrival and calculates sediment velocity; the full waveform is stored for later calculation of attenuation.

All velocity data reported here are corrected for in situ temperature and pressure using the following (Wyllie et al., 1956):

$$1/V_{corr} = 1/V_{meas} + [(\eta/V_{in\ situ}) - (\eta/V_{lab})], \quad (8)$$

where V_{corr} = corrected velocity, V_{meas} = measured velocity, $V_{in\ situ}$ = calculated velocity of seawater at in situ temperature and pressure (using Wilson, 1960); and V_{lab} = the calculated velocity of seawater at the laboratory temperature and pressure (using Wilson, 1960). Periodically, the separation was evaluated by running a calibration procedure in distilled water. A value of sound velocity in distilled water was determined (based on standard equations) for the measured temperature and the transducer separation was calculated from signal traveltime.

The Hamilton Frame (HF) velocimeter was used to measure compressional-wave velocities at a signal frequency of 500 kHz in discrete sediment samples for which induration made it difficult to insert the DSV transducers without cracking the sample and in lithified sediments when insertion became impossible. Samples were cut carefully using a double-bladed diamond saw. Sample thickness was measured directly from the velocimeter-frame lead screw through a linear resistor output to a digital multimeter. Delays for the transducers were estimated by linear regression of traveltime vs. distance for a series of aluminum and lucite standards. Filtered seawater was used to improve the acoustic contact between the sample and the transducers. The DSV oscilloscope and processing software were used to digitize waveforms, calculate velocities, and store the waveforms. The routine procedure of measurement was to propagate the waveform parallel to the core axis (longitudinal) and across the core, parallel to the split surface (horizontal or transverse). This approach provides a measure of the acoustic anisotropy within the sediments.

Acoustic anisotropy (A_p) is calculated following the definition of Carlson and Christensen (1977):

$$A_p = 200 \times [(V_{pt} - V_{pl})/(V_{pt} + V_{pl})] \tag{9}$$

where V_{pl} = *P*-wave velocity measured in the direction parallel to the core length (longitudinal), and V_{pt} = *P*-wave velocity measured perpendicular to the core length (transverse). This definition results in a nondimensional index of acoustic anisotropy and is reported as a percentage.

Undrained Shear Strength

The undrained shear strength (S_u) of the sediment was determined using the ODP motorized miniature vane shear device following the procedures of Boyce (1976). The vane rotation rate was set to 50°/min. Measurements were made only in the fine-grained units from soft to very stiff consistencies. The vane used for all measurements has a 1:1 blade ratio with a dimension of 1.27 cm.

The instrument measures the difference in rotational strain between the top and bottom of the linear spring using digital shaft encoders. The rotational strains are used to compute torque and strain and are recorded on a PC-compatible computer. After Site 927, the data were recorded on a new software package on a Macintosh computer. The shear strength reported is the peak strength determined from the torque vs. strain plot. In addition to the peak shear strength, at selected intervals, the residual strength was determined from the same plot where the failure was not dominated by cracking of the sample (Pyle, 1984).

In the analyses of vane tests, the assumption is made that a cylinder of sediment is uniformly sheared about the axis of the vane in an undrained condition, with cohesion as the principal contributor to shear strength. Departures from this assumption include progressive cracking within and outside of the failing specimen, uplift of the failing core cylinder, drainage of local pore pressures (i.e., the test can no longer be considered to be undrained), and stick-slip behavior.

In some sediments, where progressive cracking occurred before failure, measurements were made using the pocket penetrometer. The pocket penetrometer is a small, flat-footed cylindrical probe that is pushed into the split core 6.4 mm. The resulting resistance is the unconfined compressive strength or 2 S_u. A scale directly reads out in units of kg/cm^2. The values of unconfined compression are converted to values of S_u and are reported in units of kPa.

Electrical Resistivity

Two different probes are used to measure electrical resistivity of the sediment. Each probe has the same configuration, comprising two current and two potential electrodes (Wenner spread). The probes differ in their electrode spacing. The ODP probe has a small electrode spacing (0.15 mm) that makes it more suitable for measurement in stiff sediment, whereas the Scripps Institution of Oceanography (SIO) probe has a spacing of 10 mm and is suitable for soft sediment. Both probes are used in the same manner, that is, by applying an alternating current to the two outer electrodes and measuring a potential drop across the two inner electrodes.

The resistance of the saturated sediment is determined from the potential drop in millivolts. The potential is converted to resistance by dividing by the instrument current. The resistance is then converted to resistivity by multiplying by the instrument cell constant. The cell constant is defined as the cross-sectional area divided by the length between the two voltage electrodes. The cell constant was determined for each instrument by measuring the resistance of a known fluid (seawater) at controlled temperatures.

Electrical resistivity of the sediments was measured by pushing the electrodes approximately 2 mm into the split-core surface. Measurements were made with the probes aligned across the core diameter. These measurements were used to determine formation factor and to estimate porosity. Formation factor (F) is the ratio of the resistivity of the saturated sediment to the resistivity of the pore fluid. Porosity of the sediment was estimated from the formation factor following a modified Archie equation (Lovell, 1984), as follows:

$$\mathrm{F} = a\,\eta^{-m}, \tag{10}$$

where a and m = coefficients that vary with sediment type, and η = porosity. The coefficients for each lithology were determined by plotting F vs. measured porosity and fitting an exponential to these data, assuming a constant value for the cementation coefficient (m).

Thermal Conductivity

The thermal conductivity of cored material was measured using the needle probe method, in full-space configuration for soft sediments (Von Herzen and Maxwell, 1959). All measurements were made after the cores had equilibrated to the laboratory temperature. Data are reported in units of W/(m·K) and have an estimated error of 5%–10%. Measurement methods used on Leg 154 closely follow those used on Leg 146 (Shipboard Scientific Party, 1994). For each measurement, a probe is inserted into the whole core and then is heated while the temperature is measured. From these data, a least-squares technique is applied as follows:

$$T(t) = (q/4\pi_k) \times \ln(t) + L(t), \tag{11}$$

where k = apparent thermal conductivity, T = temperature, t = time, and q = heat input per unit length of wire per unit time. The term $L(t)$ describes a linear change in temperature with time; it includes the background temperature drift and any linearity that results from instrumental errors and the geometrical inadequacies of the experiment. All measurements were corrected for a linear offset between measured and true thermal conductivities, determined from a series of tests with standards of known conductivities.

Thermal conductivity probes were calibrated by conducting measurements on three standards—red rubber, fused silica, and macor ceramic—which have known thermal conductivities of 0.96, 1.38, and 1.61 W/(m·K), respectively. The linear regression of known thermal conductivity, k_{corr}, to probe reading, K_{meas}, results in a correction (Fig. 11). This correction was applied to all readings made during Leg 154.

DOWNHOLE MEASUREMENTS

Introduction

Downhole logs are used to characterize the geophysical, geochemical, and structural properties of a drilled sequence. Log data offer several advantages over core-based analyses in that they are rapidly collected and represent continuous, in situ measurements of the formation. Combined core-log research efforts can potentially integrate the ground-truth information provided by detailed core analyses with continuous and multivariate log data. Because of shipboard composite section development and the implementation of new high-resolution logging techniques available through the new Schlumberger MAXIS 500 logging system, Leg 154 represents one of the best opportunities in the history of ODP to test the usefulness of log measurements for paleoclimate research.

After coring was completed, the hole was flushed of debris and a combination of sensors was lowered downhole on a 7-conductor

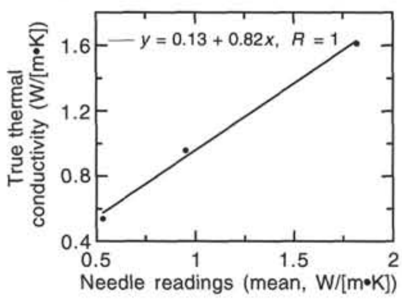

Figure 11. Calibration curve and the linear regression from the thermal conductivity standards used during Leg 154. The standards are red rubber (lowest conductivity), fused silica (middle range conductivity), and macor ceramic (highest conductivity).

cable. A wireline heave motion compensator was employed during rough seas to minimize the effect of ship heave on the tool position in the borehole. The sensors continuously monitor geophysical, geochemical, or structural properties of the formation, which are recorded typically at 15-cm depth increments by the Schlumberger MAXIS 500 or Cyber Service Unit (CSU) computers. The information depths of investigation and vertical resolutions are sensor-dependent, but they typically range from 50 to 100 cm. Four different Schlumberger tool strings were used on Leg 154: (1) a seismic stratigraphic tool string, (2) a lithoporosity tool string, (3) the Formation MicroScanner (FMS), and (4) the geochemical tool string. Also used was the geological high-sensitivity magnetic tool (GHMT-A), which was developed jointly by the French Atomic Energy Commission (CEA), TOTAL, and Schlumberger. A schematic diagram of these five tool strings is shown in Figure 12. The first two tool strings frequently are combined to form the Quad combination tool string. The Lamont-Doherty temperature tool was attached to the base of each tool string to monitor borehole temperature variations.

Shipboard Log Processing

Quad Combination Tool String

The Quad combination tool string employed on Leg 154 comprises five sensors: (1) the natural gamma spectrometry tool (NGT), (2) the phasor dual-induction tool (DIT), (3) the long-spacing digital sonic tool (SDT), (4) the high-temperature lithodensity tool (HLDT), and (5) the compensated neutron porosity tool (CNT-G). The Quad combination tool string is designed to measure compressional-wave velocity; the deep, intermediate, and shallow resistivity; and formation density and porosity in a single logging pass. Sonic velocity data are combined with density measurements to calculate an impedance log and generate synthetic seismograms for the logged sequence. The natural gamma tool (NGT) is run on this and all other tool strings to provide a common basis for log correlations. The maximum logging speed for this tool string is 600 m/hr.

The DIT provides three measurements of electrical resistivity, all with different radial depths of investigation. Two induction devices ("deep" and "medium" resistivity) send high-frequency alternating current through transmitter coils, creating a magnetic field that induces a secondary (Foucault) current in the formation. This ground-loop current produces a new inductive signal, proportional to the conductivity of the formation. This inductive signal is recorded by a series of receiving coils and is then converted to resistivity values. A third device, the spherically focused resistivity tool (SFL), measures the current necessary to maintain a constant voltage drop across a fixed interval. Vertical resolution is 2 and 1.5 m, respectively, for the deep and medium induction tools and 0.75 m for the SFL. The data are corrected for irregularities in borehole diameter. Like the HLDT density tool, the induction resistivity tools can be run in high-resolution mode. Real-time phasor processing enhances the SFL tool's intrinsic resolution and sample density increases from 15 to 2.5 cm, respectively.

Resistivity is a function of the inverse square root of porosity (Archie, 1942). Fluid salinity, clay content, hydrocarbon content, and temperature also are important factors influencing electrical resistivity. Other factors that may affect the measured resistivity are the concentration of hydrous and metallic minerals, formation porosity, and the geometry of the pore space. The Leg 154 resistivity logs are mainly reflecting variations in sediment porosity associated with changes in sediment composition and burial compaction.

The SDT records the time required for sound to travel along the borehole wall from one of two acoustic transmitters to two receivers over source-receiver distances of 2.4, 3.0, and 3.6 m. First arrivals for the individual source-receiver paths are used to calculate sonic velocities; four velocity values are measured at each depth along four possible paths. Only compressional-wave velocities are determined on board ship, but the full sonic waveforms are recorded for post-cruise processing to determine shear wave and Stoneley wave velocities. Logs can be corrected for cycle skipping (where the receiver misses the first arrival and responds to that of the second signal) using the fourfold measurement redundancy. Compressional-wave velocity is controlled primarily by porosity and lithification; decreases in porosity and increases in consolidation and lithification typically result in velocity increases with depth in a sedimentary deposit.

The HLDT uses a ^{137}Ce source of 0.66 MeV gamma rays for formation bulk-density measurement. The source is mounted in the tool body, and an eccentralizing arm presses it and a pair of detectors against the borehole wall. Determination of density is based on the theory of Compton scattering of gamma rays within the formation, which is a function of electron density. The electron density is converted to bulk density on the assumption that most rock-forming elements have atomic weights that are twice their atomic numbers.

In addition, the lithodensity tool records a photoelectric effect index. Photoelectric absorption occurs in the energy window below 150 MeV and is principally dependent upon the energy of the incident gamma ray and the atomic cross section. The measurement is independent of porosity and therefore can be used as a matrix lithology indicator. The density and photoelectric effect measurements require good contact between the sensor and borehole wall; the tool measures the "standoff" and corrections can be made for excessive borehole roughness. The intrinsic vertical resolution of the tool is approximately 0.45 m, although a recent analysis of core and log density data from Leg 138 suggests that the real resolution is closer to 0.8 m (Harris et al., in press).

The HLDT can be run in high-resolution mode, which substantially improves measurement resolution. Logging speed must be reduced to 300 m/hr, and the resulting data are processed in real-time (alpha-processing) to take dual advantage of the near detector-source spacing (15 cm) and the far detector measurement stability. The sample measurement interval is reduced from the standard 15 cm to 2.5 cm, and the intrinsic resolution approaches the near detector spacing (15 cm). Excellent hole conditions are the main prerequisite for high-resolution logging to be of value.

The CNT-G uses a 16 curie Am-Be neutron source and two pairs of thermal and epithermal detectors to measure hydrogen abundance, which, in turn, is recalculated as porosity. Energy loss by incident high energy neutrons depends largely on the concentration of hydrogen in the formation as the neutrons and hydrogen atoms have nearly equal mass. Within a few microseconds, the neutrons have been slowed down to thermal velocities and are captured by other atomic nuclei such as Si or Ca. The total hydrogen content of the formation is determined by the flux ratio of emitted to detected neutrons. Free water content (porosity) is determined from the thermal neutron counts. Water that is structurally bound (e.g., clay minerals) can be estimated by subtracting free water from the total water estimates. The tool is designed to be run eccentered in the borehole, so CNT-G

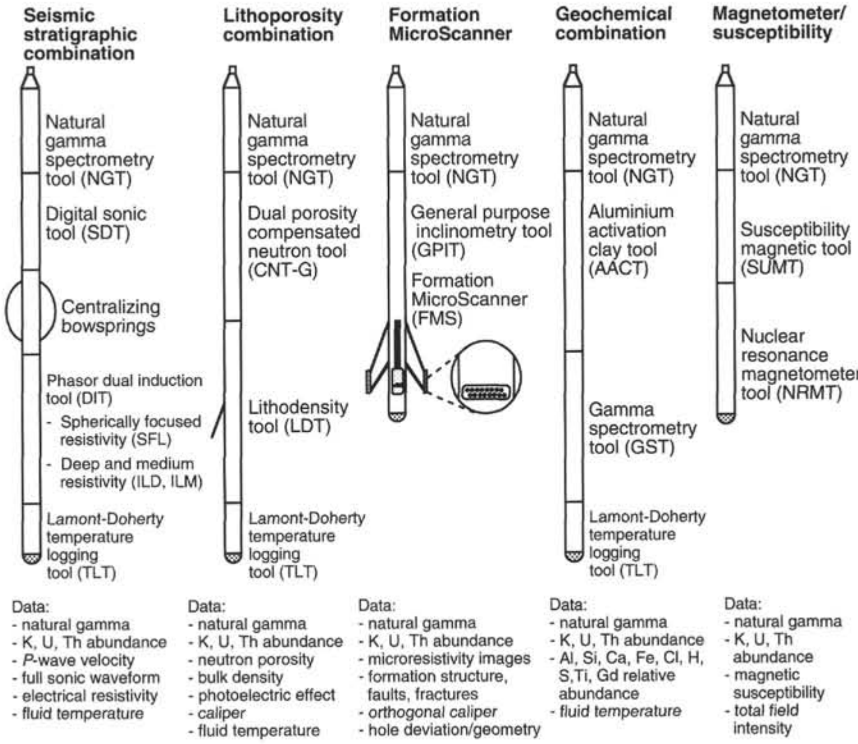

Figure 12. Schematic diagram of Schlumberger logging tool strings used on Leg 154. Tool strings are not drawn to relative scale.

data from Quad runs (where the tool is not fully eccentered) should be interpreted with caution. Tool resolution is approximately 45 cm.

Geochemical Tool String

The geochemical tool string used on Leg 154 includes an NGT, an aluminum activation clay tool (AACT), and a gamma-ray spectrometry tool (GST) (Hertzog et al., 1989). Relative concentrations of Si, Ca, Fe, S, H, and Cl and wet weight percents of K, U, Th, and Al are determined on board ship. Extensive additional shore-based processing is required to obtain dry weight percentages of the above elements, at which stage Gd and Ti are also determined. The tool string is logged at 200 m/hr. The NGT measures the natural radioactivity of the formation (Lock and Hoyer, 1971). The majority of natural gamma rays are emitted by ^{40}K and by U and Th isotopes and their daughter products. Near-field (i.e., near the borehole wall) natural gamma emissions of the formation are measured by a NaI scintillation detector mounted inside the sonde. The energy spectrum measured by the detector is divided into five discrete energy windows. At each 15-cm sample interval, the total counts recorded in each window are processed to give elemental abundances of K, U, and Th. The depth of investigation is about 0.3–0.5 m. The NGT is positioned at the top of the tool string, thereby measuring the natural radioactivity before the formation is irradiated by the sources in the tools below.

K, U, and Th are generally most abundant in clay minerals, so the gamma-ray log is commonly used as an estimate of the clay content of the formation. Silicic volcaniclastic material and K-feldspar-rich rocks also can have high concentrations of these three elements, so interpretations must be tied to the core lithology. At some sites, the U log closely follows variations in organic carbon content.

The AACT forms the second part of the geochemical tool string measuring the concentration of Al in the formation by delayed neutron activation (Scott and Smith, 1973). When the natural isotope ^{27}Al absorbs a thermal neutron derived from the 2.5 MeV ^{252}Cf source of the AACT, it forms an unstable ^{28}Al atom with a half-life of about 2 min. When the unstable nucleus decays (to ^{28}Si), a gamma ray with a characteristic energy (1779 KeV) is emitted and subsequently detected by the AACT. Because the AACT simultaneously counts the natural gamma radiation of the formation, the net Al spectrum is determined by subtracting the count rates from the NGT, which is positioned above the AACT in the tool string.

The GST consists of a pulsed 14 MeV neutron generator and a NaI scintillation detector. Incident neutrons lose energy through inelastic scattering interactions and, on reaching thermal energy levels, are captured by elemental nuclei. Characteristic gamma rays are emitted upon neutron capture; these gamma rays and their relative energy levels are recorded by the tool. The 256-channel energy spectrum is deconvolved to determine relative abundances of Ca, Si, Fe, Cl, H, and S on board ship. Post-cruise processing of the GST data provided the additional elemental yields of Gd and Ti. The above yields (except Cl and H) are then combined with elements determined from the NGT and AACT to derive the dry weight percentages of the elements Si, Ca, Fe, S, Ti, K, and Al, in addition to Gd, Th, and U in ppm. An estimate of (Mg + Na) can be made by using the photoelectric factor from the HLDT.

Formation MicroScanner

The Formation MicroScanner (FMS) produces high-resolution images of the microresistivity character of the borehole wall that can be used for detailed sedimentological and/or structural interpretations (Ekstrom et al., 1986). The FMS tool comprises 16 electrode "buttons" on four orthogonal pads that are pressed against the borehole wall. The electrodes are spaced approximately 2.5 mm apart and are arranged in two diagonally offset rows of eight electrodes each. Processing corrects the offset rows to one level, doubling the horizontal resolution to approximately 1.25 mm. The FMS tool string contains a general purpose inclinometry tool (GPIT) that orients the resistivity measurements through the use of an accelerometer and magnetometer information on the declination and inclination of the Earth's magnetic field. The tool string includes an NGT to enable correlation of the FMS to other tool strings. Using the new Maxis 500 logging unit, the raw data are processed real-time during logging to transform individual microresistivity traces into complete, oriented images. Full color images are immediately available. Scientific applications of the FMS images include detailed correlation of coring and logging depths, core orientation, and mapping of fractures, faults, foliations, and other formation structures as well as determination of strikes and dips of bedding planes.

The Lamont Doherty Temperature Tool

The LDEO temperature logging tool (TLT) is a self-contained tool that can be attached to the base of any of the sensor combinations. Data from two thermistors and a pressure transducer are collected every 1 s and are recorded internally. Once the in situ measurement is completed, the data are transferred to a shipboard computer for analysis. The fast-response thermistor, though less accurate, is able to detect small abrupt temperature excursions caused by fluid flow from the formation. The slow-response thermistor is more accurate and can be used to estimate the temperature gradient. Data are recorded as a function of time, with conversion to depth based on the pressure transducer. The TLT measures the borehole water temperature, not the true formation temperature; it is common to observe gradual borehole warming (thermal rebound) as logging proceeds. The TLT data are not representative of the true thermal gradient and, hence, should not be used in heat-flow calculations. For Leg 154, the TLT data are primarily used for calculation of borehole fluid resistivities for log porosity estimates.

Geological High-sensitivity Magnetic Tool

High-sensitivity total magnetic field and susceptibility logging tools were deployed on Leg 154 to test the effectiveness of these tools in resolving borehole magnetic polarity transitions and susceptibility variations. Similar tools were run previously on Legs 134 and 145. These tools were developed jointly by oil industry (TOTAL and Schlumberger) and French government research institutions (CEA-LETI and CNRS-ENS). The tools were designed and constructed by a branch of the French Atomic Energy Commission (CEA-LETI), which also developed the analysis software.

Magnetic induction, B, in a borehole depends on location p and time t with (Pozzi et al., 1988)

$$B(p,t) = Br(p) + Ba(p) + Bf(p) + Bt(p,t), \quad (12)$$

where $Br(p)$ = the regular inner field and $Ba(p)$ = the anomaly field related to large-scale heterogeneities in susceptibility or magnetic remanence. In the absence of such heterogeneities, the spatial variation of both Br and Bf with depth is linear. $Bf(p)$ is the induction caused by the magnetization (induced and remanent) of the sediments around the borehole; it can easily be separated from $Br(p)$ and $Ba(p)$. $Bt(p,t)$ is time dependent and represents the induction caused by transient variations of the Earth's field. The time-dependent component can be reduced using a radio-linked reference, or it can be estimated by repeat sections. To obtain direct magnetostratigraphy from $Bf(p)$, the susceptibility and total field measurements are combined to discriminate the induced and remanent magnetizations. Specifications of the probes such as impulse response, calibration ratio, and geomagnetic location of the hole are used to calculate the susceptibility effect on the scalar total field magnetometer. The result of calculations is the scalar remanent magnetization.

The nuclear resonance magnetometer tool (NRMT) can be used in borehole temperatures up to 125°C; however, the probe used for Leg 154 is more precise and has a maximum operating temperature of 65°C. The average precision of this tool is 0.5 nT based on repeat sections. The susceptibility magnetic tool (SUMT) employs a classic measurement principle that detects the mutual induction signal between two coils (0.8 m apart) caused by the surrounding borehole lithology. The excitation frequency is about 200 Hz. The precision between repeated sections is generally better than 3 ppm (3×10^{-6} SI). Both tools are housed in nonmagnetic materials; tools are logged at 600 m/hr and the data are recorded every 5 cm.

Shore-based Log Processing

Additional log processing and display were performed at each of the six sites by the Borehole Research Group (BRG) at LDEO, IMT, and Leicester University, using Schlumberger "Logos" software and additional programs developed by members of the BRG. Displays of most of these processed data appear with accompanying text at the end of the appropriate site chapters in this volume. Files of all processed logs (including FMS, dipmeter, BRG temperature, and high-resolution density and neutron data not shown in printed form) plus explanatory texts are included on the CD-ROM disc enclosed in the back pocket of this volume; a directory of the contents of the disc is found at the front of this volume.

Shore-based processing of data from each hole consisted of (1) depth adjustments of all logs to a common measurement below the seafloor, (2) corrections specific to certain tools, and (3) quality control and rejection of unrealistic values.

The depth-shifting procedure is based on an interactive, graphical depth-match program that allows the processor to correlate logs visually and to define appropriate shifts. The reference log and the log to be adjusted in depth are displayed side by side on a screen, and vectors connect the two at positions chosen by the user. The total gamma-ray curve (SGR) from the NGT tool run on each logging string was used in most cases to correlate the logging runs. In general, the reference curve is chosen on the basis of constant, low cable tension and high cable speed (tools run at faster speeds are less likely to stick and are less susceptible to data degradation caused by ship heave). Other factors, however, such as the length of the logged interval, the presence of drill pipe, and the statistical quality of the collected data (better statistics are obtained at lower logging speeds) are also considered in the selection. A list of the amount of differential depth shifts applied at each hole is available upon request to BRG (LDEO).

Specific tool corrections were performed on the gamma-ray data to account for changes in borehole size and for the composition of the drilling fluid. Processing techniques unique to the AACT and GST tools of the geochemical string are described in detail below.

Quality control was performed by cross-correlation of all logging data. If the data processor concluded that individual log measurements represented unrealistic values, the choices were to discard the data outright and substitute the null value of "–999.25," or to identify a specific depth interval containing suspect values that must be used with caution. The latter are noted in the text that accompanies all processed log displays. Quality control of the SDT acoustic data was based on discarding any of the four independent transit time measurements that were negative or that fell outside a range of reasonable values selected by the processor.

Locally, some intervals of log data appeared unreliable (usually because of poor hole conditions) and were not processed beyond what had been done on board the ship. In general, a large (>12 in.) and/or irregular borehole affects most recordings, particularly those that require eccentralization (CNT-G, HLDT) and a good contact with the borehole wall. Hole deviation can also degrade the data; the FMS, for example, is not designed to be run in holes that are more than 10° off vertical, as the tool weight might cause the caliper to close.

Onshore Geochemical Log Processing

The well-log data from the Schlumberger tools are transmitted digitally up a wireline and are recorded and processed on the *JOIDES Resolution* in the Schlumberger Cyber Service Unit (CSU). The results from the CSU are made available as "field logs" for initial shipboard interpretation. Subsequent reprocessing is necessary to correct the data for the effects of fluids added to the well, logging speed, borehole size, and drill-pipe interference. Processing of the spectrometry data is required to transform the relative elemental yields into oxide weight fractions.

The processing is performed with a set of log-interpretation programs written by Schlumberger that have been slightly modified to account for the lithologies and hole conditions encountered in ODP holes. The processing steps are summarized below.

Step 1: Reconstruction of Relative Elemental Yields from Recorded Spectral Data

This first processing step compares the measured spectra from the GST with a series of "standard" spectra to determine the relative contribution (or yield) of each element. These "standards" approximate the spectrum of each element. Using a weighted, least-squares inversion method, the relative elemental yields are calculated at each depth level.

Six elemental standards (Si, Fe, Ca, S, Cl, and H) are used to produce the shipboard yields, but three additional standards (Ti, Gd, and K) can be included in the post-cruise processing to improve the fit of the spectral standards to the measured spectra (Grau and Schweitzer, 1989). Although Ti, Gd, and K often appear in the formation in very low concentrations, they can make a large contribution to the measured spectra because they have large neutron-capture cross sections. For example, the capture cross section of Gd is 49,000 barns, whereas that of Si is 0.16 barns (Hertzog et al., 1989). Therefore, including Gd is necessary when calculating the best fit of the standard spectra to the measured spectrum.

The elemental standards (Si, Ca, Fe, Ti, Gd, Cl, and H) were used in the spectral analysis step for Holes 926B and 929E. The spectral standards for S and K were not used because these elements exist in concentrations below the detection resolution of the tool in these holes; its inclusion in the spectral inversion was found to increase the noise level significantly in the other elemental yields. The concentration of K, however, is later determined from the NGT data. A linear 10-point (5 ft, 1.52 m) moving average was applied to the output elemental yields to increase the signal-to-noise ratios.

Step 2: Depth Shifting

Geochemical processing involves the integration of data from the different tool strings; consequently, it is important that all the data are depth-correlated to one reference logging run. The NGT, run on each of the logging tool strings, provides a spectral gamma-ray curve with which to correlate each of the logging runs. A reference run is chosen on the bases of constant and low cable tension, and high cable speed (tools run at faster speeds are less likely to stick and are less susceptible to data degradation caused by ship heave). The depth-shifting procedure involves picking a number of reference points based on similar log character and then invoking a program that expands and compresses the matching logging run to fit the reference logging run. The main run of the quad combination tool string was chosen as the reference run both in Holes 926B and 929E.

Step 3: Calculation of Total Radioactivity and Th, U, and K Concentrations

The third processing routine calculates the total natural gamma radiation in the formation, as well as concentrations of Th, U, and K, using the counts in five spectral windows from the NGT (Lock and Hoyer, 1971). This routine resembles shipboard processing; however, the results were improved during post-cruise processing by including corrections for hole-size changes and temperature variations. A Kalman filtering (Ruckebusch, 1983) is used in the MAXIS unit processing at sea to minimize the statistical uncertainties in the logs, which can otherwise create erroneous negative values and anticorrelations (especially between Th and U). An alpha filter is available on shore and is recommended by Schlumberger for shore-based processing. This filter strongly smooths the raw spectral counts but keeps the total gamma-ray curve unsmoothed before calculating out the Th, U, and K. The outputs of this program are K (wet wt%), U (ppm), and Th (ppm), as well as total gamma ray and computed gamma ray (total gamma ray minus U contribution).

Step 4: Calculation of Al Concentration

The fourth processing routine calculates the concentration of Al in the formation using recorded gamma-ray data from four energy windows on the AACT. During this step, corrections are made for natural radioactivity, borehole-fluid neutron-capture cross section, formation neutron-capture cross section, formation slowing-down length, and borehole size.

Porosity and density logs are needed as inputs into this routine to convert the wet-weight percentages of K and Al curves to dry-weight percentages. Porosity logs were calculated from the deep induction and bulk density logs in Holes 926B and 929E. The comparison of log-derived porosities with shipboard core measurements provided only fair correlation in both wells. As a result, the porosity curve used in the geochemical processing consisted of interpolated core measurements, which were numerous, and comprehensively covered the logged section of both Holes 926B and 929E.

A correction is also made for Si interference with Al; the ^{252}Cf source activates the Si, producing the aluminum isotope ^{28}Al (Hertzog et al., 1989). The program uses the Si yield from the GST to determine the Si background correction. The program outputs dry-weight percentages of Al and K, which are combined in the next processing step with the GST-derived elemental yields in the oxide closure model.

The output Al in Hole 929E showed numerous high "spikes" in the upper, more rugose portion of the hole where washouts were more prevalent. In such sediments, a correlation is broadly expected between the concentrations of Al and K (representing a terrigenous component), and there were no such spikes in K at the corresponding intervals. Neutron simulation studies in previous work (Bristow, 1993) have shown that the AACT data quality is susceptible to tool standoff, typically induced by a rugose borehole. In addition, any tool sticking causes an uneven radiation of the hole; for these reasons the Al spikes in Hole 929E were considered erroneous. Any error in the weight percentages of Al is propagated into the other GST-derived elements (because of the nature of the GST elements being normalized to 100% – [Al + K]; see Eq. 14 below). To avoid propagation of this error, the spikes in the Al data were removed by interpolation. The Hole 929 wt% Al were despiked at 156, 162, 180, 192, 211, 218, 223, 272, 275, and 285 mbsf.

Step 5: Normalization of Elemental Yields from the GST to Calculate the Elemental Weight Fractions

Relative concentrations of the GST-derived elemental yields can be determined by dividing each elemental yield by a relative spectral sensitivity factor (S_i). This factor is principally related to the thermal neutron-capture cross sections and also to its gamma-ray production and detection probability of each element (Hertzog et al., 1989). The relative elemental concentrations are related to absolute concentrations by a depth-dependent normalization factor (F), as defined by the relationship:

$$Wt_i = FY_i/S_i \tag{13}$$

where Wt_i = absolute elemental concentration, and Y_i = relative elemental yield. The normalization factor is calculated on the basis that the sum of all the elemental weight fractions is unity (100%). The closure model handles the absence of carbon and oxygen, which are not measured by this tool string, with the approximation that each of the measurable elements combines with a known oxide or carbonate (Table 6).

Table 6. Oxide factors used in normalizing elements to 100% and converting elements to oxides.

Element	Oxide/carbonate	Conversion factor
Si	SiO_2	2.139
Ca	CaO	2.497
Fe	FeO*	1.358
K	K_2O	1.205
Ti	TiO_2	1.668
Al	Al_2O_3	1.889

The dry weight percentages of Al and K are normalized with the reconstructed elemental yields to the determine the normalization factor at each depth interval from the following equation:

$$F(\Sigma_i X_i Y_i / S_i) + X_K Wt_K + X_{Al} Wt_{Al} = 100, \qquad (14)$$

where X_i = oxide factor (atomic weight of the associated oxide or carbonate of element i atomic weight of element i; X_K = oxide factor (atomic weight K_2O atomic weight of K); Wt_K = dry wt% of K as determined from the NGT; X_{Al} = oxide factor; (atomic weight of Al_2O_3 atomic weight of Al); and Wt_{Al} = dry wt% of corrected Al. The value X_i accounts for the C and O associated with each element.

Step 6: Calculation of Oxide Percentages

This routine converts the elemental weight percentages into oxide percentages by multiplying each by its associated oxide factor, as shown in Table 6.

Step 7: Calculation of Error Logs

The statistical uncertainty of each element is calculated for each of the elements measured with the GST and NGT (Grau et al., 1990; Schweitzer et al., 1988). This error is strongly related to the normalization factor, which is calculated at each depth level (Eq. 13).

REFERENCES*

Archie, G.E., 1942. The electrical resistivity log as an aid in determining some reservoir characteristics. *J. Pet. Tech.,* 5:1–8.

ASTM, 1989. *Annual Book of ASTM Standards for Soil and Rock; Building Stones: Geotextiles* (Vol. 04.08): Philadelphia (Am. Soc. Testing Materials).

Aubry, M.-P., Berggren, W.A., Kent, D.V., Flynn, J.J., Klitgord, K.D., Obradovich, J.D., and Prothero, D.R., 1988. Paleogene geochronology: an integrated approach. *Paleoceanography,* 3:707–742.

Backman, J., 1986. Late Paleocene to middle Eocene calcareous nannofossil biochronology from the Shatsky Rise, Walvis Ridge and Italy. *Palaeogeogr., Palaeoclimatol., Palaeoecol.,* 57:43–59.

————, 1987. Quantitative calcareous nannofossil biochronology of middle Eocene through early Oligocene sediment from DSDP Sites 522 and 523. *Abh. Geol. Bundesanst. (Austria),* 39:21–31.

Backman, J., Schneider, D.A., Rio, D., and Okada, H., 1990. Neogene low-latitude magnetostratigraphy from Site 710 and revised age estimates of Miocene nannofossil events. *In* Duncan, R.A., Backman, J., Peterson, L.C., et al., *Proc. ODP, Sci. Results,* 115: College Station, TX (Ocean Drilling Program), 271–276.

Backman, J., and Shackleton, N.J., 1983. Quantitative biochronology of Pliocene and Pleistocene calcareous nannoplankton from the Atlantic, Indian and Pacific Oceans. *Mar. Micropaleontol.,* 8:141–170.

Berggren, W.A., 1969. Paleogene biostratigraphy and planktonic foraminifera of Northern Europe. *Proc. First Int. Conf. Planktonic Microfossils, Geneva, 1967:* Leiden (E.J. Brill), 1:121–160.

Berggren, W.A., Kent, D.V., and Flynn, J.J., 1985a. Jurassic to Paleogene: Part 2. Paleogene geochronology and chronostratigraphy. *In* Snelling, N.J. (Ed.), *The Chronology of the Geological Record.* Geol. Soc. London Mem., 10:141–195.

*Abbreviations for names of organizations and publications in ODP reference lists follow the style given in *Chemical Abstracts Service Source Index* (published by American Chemical Society).

Berggren, W.A., Kent, D.V., Flynn, J.J., and Van Couvering, J.A., 1985b. Cenozoic geochronology. *Geol. Soc. Am. Bull.,* 96:1407–1418.

Berggren, W.A., Kent, D.V., and Swisher, C.C., III, in press. A revised Cenozoic geochronology and chronostratigraphy. *In* Berggren, W.A., Kent, D.V., and Hardenbol, J. (Eds.), *Geochronology, Timescales and Correlation: Framework for an Historical Geology.* Spec. Publ.—Soc. Econ. Paleontol. Mineral.

Berggren, W.A., Kent, D.V., and Van Couvering, J.A., 1985c. The Neogene: Part 2. Neogene geochronology and chronostratigraphy. *In* Snelling, N.J. (Ed.), *The Chronology of the Geological Record.* Geol. Soc. London Mem., 10:211–260.

Berggren, W.A., and Miller, K.G., 1988. Paleogene tropical planktonic foraminiferal biostratigraphy and magnetobiochronology. *Micropaleontology,* 34:362–380.

Berggren, W.A., and Norris, R.D., 1993. Origin of the genus *Acarinina* and revisions to Paleocene biostratigraphy. *Geol. Soc. Am. Abstr. Progr.,* A-359.

Blow, W.H., 1969. Late middle Eocene to Recent planktonic foraminiferal biostratigraphy. *Proc. First. Int. Conf. Planktonic Microfossils, Geneva, 1967:* Lieden (E.J. Brill), 1:199–422.

————, 1979. *The Cainozoic Globigerinida:* Leiden (E.J. Brill).

Bolli, H.M., and Premoli Silva, I., 1973. Oligocene to Recent planktonic foraminifera and stratigraphy of the Leg 15 sites in the Caribbean Sea. *In* Edgar, N.T., Saunders, J.B., et al., *Init. Repts. DSDP,* 15: Washington (U.S. Govt. Printing Office), 475–497.

Bolli, H.M., and Saunders, J.B., 1985. Oligocene to Holocene low latitude planktic foraminifera. *In* Bolli, H.M., Saunders, J.B., and Perch-Nielsen, K. (Eds.), *Plankton Stratigraphy:* Cambridge (Cambridge Univ. Press), 155–262.

Boyce, R.E., 1976. Definitions and laboratory techniques of compressional sound velocity parameters and wet-water content, wet-bulk density and porosity parameters by gravimetric and gamma-ray attenuation techniques. *In* Schlanger, S.O., Jackson, E.D., et al., *Init. Repts. DSDP,* 33: Washington (U.S. Govt. Printing Office), 931–958.

Bralower, T.J., Zachos, J.C., Thomas, E., Parrow, M., Paull, C., Kelly, D.C., Premoli Silva, I., and Sliter, W.V., in press. Stable isotope stratigraphy of Site 865, Allison Guyot: implications for Paleogene paleoceanography of the tropical Pacific Ocean. *In* Winterer, E.L., Sager, W.W., Firth, J.V., and Sinton (Eds.), *Proc. ODP, Sci. Results,* 143: College Station, TX (Ocean Drilling Program).

Bristow, J.F., 1993. Physical and chemical characteristics of rocks from downhole measurements [Ph.D. thesis]. University of Nottingham.

Bukry, D., 1973. Low-latitude coccolith biostratigraphic zonation. *In* Edgar, N.T., Saunders, J.B., et al., *Init. Repts. DSDP,* 15: Washington (U.S. Govt. Printing Office), 685–703.

————, 1975. Coccolith and silicoflagellate stratigraphy, northwestern Pacific Ocean, Deep Sea Drilling Project Leg 32. *In* Larson, R.L., Moberly, R., et al., *Init. Repts. DSDP,* 32: Washington (U.S. Govt. Printing Office), 677–701.

————, 1978. Biostratigraphy of Cenozoic marine sediment by calcareous nannofossils. *Micropaleontology,* 24:44–60.

Cande, S.C., and Kent, D.V., 1992. A new geomagnetic polarity time scale for the Late Cretaceous and Cenozoic. *J. Geophys. Res.,* 97:13917–13971.

Carlson, R.L., and Christensen, N.I., 1977. Velocity anisotropy and physical properties of deep-sea sediments from the western South Atlantic. *In* Supko, P.R., Perch-Nielsen, K., et al., *Init. Repts. DSDP,* 39: Washington (U.S. Govt. Printing Office), 555–559.

Chaisson, W.P., and Leckie, R.M., 1993. High-resolution Neogene planktonic foraminifer biostratigraphy of Site 806, Ontong Java Plateau (western equatorial Pacific). *In* Berger, W.H., Kroenke, L.W., Mayer, L.A., et al., *Proc. ODP, Sci. Results,* 130: College Station, TX (Ocean Drilling Program), 137–178.

Corliss, B.H., 1979. Recent deep-sea benthonic foraminiferal distribution in the southeast Indian Ocean: inferred bottom-water routes and ecological implications. *Mar. Geol.,* 31:115–138.

Ekstrom, M.P., Dahan, C.A., Chen, M.Y., Lloyd, P.M., and Rossi, D.J., 1986. Formation imaging with microelectrical scanning arrays. *Trans. SPWLA 27th Annu. Logging Symp.,* Paper BB.

Emeis, K.-C., and Kvenvolden, K.A., 1986. Shipboard organic geochemistry on *JOIDES Resolution. ODP Tech. Note,* 7.

Fornaciari, E., Raffi, I., Rio, D., Villa, G., Backman, J., and Olafsson, G., 1990. Quantitative distribution patterns of Oligocene and Miocene calcareous nannofossils from the western equatorial Indian Ocean. *In* Duncan, R.A., Backman, J., Peterson, L.C., et al., *Proc. ODP, Sci. Results,* 115: College Station, TX (Ocean Drilling Program), 237–254.

Gartner, S., 1992. Miocene nannofossil chronology in the North Atlantic, DSDP Site 608. *Mar. Micropaleontol.,* 18:307–331.

Gieskes, J.M., Gamo, T., and Brumsack, H.J., 1991. Chemical methods for interstitial water analysis aboard *JOIDES Resolution. ODP Tech. Note,* 15.

Grau, J.A., and Schweitzer, J.S., 1989. Elemental concentrations from thermal neutron capture gamma-ray spectra in geological formations. *Nucl. Geophys.,* 3:1–9.

Grau, J.A., Schweitzer, J.S., and Hertzog, R.C., 1990. Statistical uncertainties of elemental concentrations extracted from neutron induced gamma-ray measurements. *IEEE Trans. Nucl. Sci.,* 37:2175–2178.

Hagelberg, T., Shackleton, N., Pisias, N., and Shipboard Scientific Party, 1992. Development of composite depth sections for Sites 844 through 854. *In* Mayer, L., Pisias, N., Janecek, T., et al., *Proc. ODP, Init. Repts.,* 138 (Pt. 1): College Station, TX (Ocean Drilling Program), 79–85.

Harris, S., Hagelberg, T., Mix, A., Pisias, N., and Shackleton, N.J., in press. Sediment depths determined by comparisons of GRAPE and logging density data during Leg 138. *In* Pisias, N.G., Mayer, L.A., Janecek, T.R., Palmer-Julson, A., and van Andel, T.H. (Eds.), *Proc. ODP, Sci. Results,* 138: College Station, TX (Ocean Drilling Program).

Hertzog, R., Colson, L., Seeman, B., O'Brien, M., Scott, H., McKeon, D., Wraight, J., Grau, J., Ellis, D., Schweitzer, J., and Herron, M., 1989. Geochemical logging with spectrometry tools. *SPE Form. Eval.,* 4:153–162.

Hilgen, F.J., 1991a. Astronomical calibration of Gauss to Matuyama sapropels in the Mediterranean and implications for the Geomagnetic Polarity Time Scale. *Earth Planet. Sci. Lett.,* 104:226–244.

————, 1991b. Extension of the astronomically calibrated (polarity) time scale to the Miocene/Pliocene boundary. *Earth Planet. Sci. Lett.,* 107:349–368.

Hoppie, B.W., Blum, P., and Shipboard Scientific Party, 1994. Natural-gamma-ray measurements on ODP cores: introduction to procedures with examples from Leg 150. *In* Miller, K.G., Mountain, G.S., Blum, P., Poag, C.W., and Twitchell, D.C. (Eds.), *Proc. ODP, Init. Repts.,* 150: College Station, TX (Ocean Drilling Program), 51–59.

Keller, G., 1988. Extinction, survivorship and evolution of planktic foraminifers across the Cretaceous/Tertiary Boundary at El Kef, Tunisia. *Mar. Micropaleontol.,* 13:239–263.

Kennett, J.P., and Srinivasan, M.S., 1983. *Neogene Planktonic Foraminifera: A Phylogenetic Atlas:* Stroudsberg, PA (Hutchinson Ross).

Kvenvolden, K.A., and McDonald, T.J., 1986. Organic geochemistry on the *JOIDES Resolution*—an assay. *ODP Tech. Note,* 6.

Leckie, R.M., Farnham, C., and Schmidt, M.G., 1993. Oligocene planktonic foraminifer biostratigraphy of Hole 803D (Ontong Java Plateau) and Hole 628A (Little Bahama Bank), and comparison with the southern high latitudes. *In* Berger, W.H., Kroenke, L.W., Mayer, L.A., et al., *Proc. ODP, Sci. Results,* 130: College Station, TX (Ocean Drilling Program), 113–136.

Lock, G.A., and Hoyer, W.A., 1971. Natural gamma ray spectral logging. *Log Analyst,* 12:3–9.

Lohmann, G.P., 1978. Abyssal benthonic foraminifera as hydrographic indicators in the western South Atlantic Ocean. *J. Foraminiferal Res.,* 8:6–34.

Lovell, M.A., 1984. Thermal conductivity and permeability assessment by electrical conductivity measurements in marine sediments. *Mar. Geotechnol.,* 6:205–240.

Mackensen, A., Fütterer, D.K., Grobe, H., and Schmiedl, G., 1993. Benthic foraminiferal assemblages from the eastern South Atlantic Polar Front region between 35° and 57°S: distribution, ecology and fossilization potential. *Mar. Micropaleontol.,* 22:33–69.

Manheim, F.T., and Sayles, F.L., 1974. Composition and origin of interstitial water of marine sediments based on deep sea drilled cores. *In* Goldberg, E.D. (Ed.), *The Sea* (Vol. 5): New York (Wiley Interscience), 527–568.

Martini, E., 1971. Standard Tertiary and Quaternary calcareous nannoplankton zonation. *In* Farinacci, A. (Ed.), *Proc. 2nd Int. Conf. Planktonic Microfossils, Roma:* Rome (Ed. Tecnosci.), 2:739–785.

Mayer, L., Pisias, N., Janecek, T., et al., 1992. *Proc. ODP, Init. Repts.,* 138 (Pts. 1 and 2): College Station, TX (Ocean Drilling Program).

Mazzullo, J.M., Meyer, A., and Kidd, R.B., 1988. New sediment classification scheme for the Ocean Drilling Program. *In* Mazzullo, J., and Graham, A.G. (Eds.), *Handbook for Shipboard Sedimentologists.* ODP Tech. Note, 8:45–67.

Munsell Soil Color Charts, 1975. Baltimore, MD (Munsell Color).

Okada, H., and Bukry, D., 1980. Supplementary modification and introduction of code numbers to the low-latitude coccolith biostratigraphic zonation (Bukry, 1973; 1975). *Mar. Micropaleontol.,* 5:321–325.

————, 1991. Quantitative calcareous nannofossil biostratigraphy and biochronology of early through late Miocene sediments from DSDP Hole 608. *Medd. Stockholm Univ. Inst. Geol. Geochem.,* 203.

Olafsson, G., and Villa, G., 1992. Reliability of sphenoliths as zonal markers in Oligocene sediments from the Atlantic and Indian oceans. *In* Proto Decima, F., Monechi, S., and Rio, D. (Eds.), *Proc. Int. Nannoplankton Assoc. Conf., Firenze 1989.* Mem. Sci. Geol., 43:261–275.

Pozzi, J.P., Martin, J.-P., Pocachard, J., Feinberg, H., and Galdeano, A., 1988. In situ magnetostratigraphy: interpretation of magnetic logging in sediments. *Earth Planet. Sci. Lett.,* 88:357–373.

Premoli Silva, I., and Spezzafari, S., 1990. Paleogene planktonic foraminifer biostratigraphy and paleoenvironmental remarks on Paleogene sediments from Indian Ocean sites, Leg 115. *In* Duncan, R.A., Backman, J., Peterson, L.C., et al., *Proc. ODP, Sci. Results,* 115: College Station, TX (Ocean Drilling Program), 277–314.

Pyle, M.R., 1984. Vane shear data on undrained residual strength. *J. Geotech. Engr. Div., Am. Soc. Civ. Eng.,* 110:543–547.

Raffi, I., Backman, J., Rio, D., and Shackleton, N.J., 1993. Plio-Pleistocene nannofossil biostratigraphy and calibration to oxygen isotope stratigraphies from Deep Sea Drilling Project Site 607 and Ocean Drilling Program Site 677. *Paleoceanography,* 8:387–408.

Raffi, I., and Flores, J.A., in press. Pleistocene through Miocene calcareous nannofossils from eastern equatorial Pacific Ocean (Leg 138). *In* Pisias, N.G., Mayer, L.A., Janecek, T.R., Palmer-Julson, A., and van Andel, T.H. (Eds.), *Proc. ODP, Sci. Results,* 138: College Station, TX (Ocean Drilling Program).

Rio, D., Sprovieri, R., and Di Stefano, E., in press. The Gelasian: a proposal for a new Pliocene Stage. *Riv. Paleontol. Stratigr. Milano.*

Rio, D., Sprovieri, R., and Thunell, R., 1991. Pliocene-lower Pleistocene chronostratigraphy: a re-evaluation of Mediterranean type sections. *Geol. Soc. Am. Bull.,* 103:1049–1058.

Roth, P.H., and Thierstein, H.R., 1972. Calcareous nannoplankton, Leg 14 of the Deep Sea Drilling Project. *In* Hayes, D.E., Pimm, A.C., et al., *Init. Repts. DSDP,* 14: Washington (U.S. Govt. Printing Office), 421–485.

Ruckebusch, G., 1983. A Kalman filtering approach to natural gamma ray spectroscopy in well logging. *IEEE Trans. Autom. Control,* AC-28:372–380.

Schnitker, D., 1974. West Atlantic abyssal circulation during the past 120,000 years. *Nature,* 248:385–387.

————, 1980. Quaternary deep-sea benthic foraminifers and bottom water masses. *Annu. Rev. Earth Planet. Sci.,* 8:343–470.

Schweitzer, J.S., Grau, J.A., and Hertzog, R.C., 1988. Precision and accuracy of short-lived activation measurements for in situ geological analyses. *J. Trace Microprobe Techniques,* 6:437–451.

Scott, H.D., and Smith, M.P., 1973. The aluminum activation log. *Log Analyst,* 14:3–12.

Shackleton, N.J., Berger, A., and Peltier, W.R., 1990. An alternative astronomical calibration of the lower Pleistocene time scale based on ODP Site 667. *Trans. R. Soc. Edinburgh, Earth Sci.,* 81:251–261.

Shackleton, N.J., Crowhurst, S., Hagelberg, T., Pisias, N.G., and Schneider, D.A., in press. A new late Neogene time scale: application to Leg 138 sites. *In* Pisias, N.G., Mayer, L.A., Janecek, T.R., Palmer-Julson, A., and van Andel, T.R. (Eds.), *Proc. ODP, Sci. Results,* 138: College Station, TX (Ocean Drilling Program).

Shipboard Scientific Party, 1994. Explanatory notes. *In* Westbrook, G.K., Carson, B., Musgrave, R.J., et al., *Proc. ODP, Init. Repts.,* 146 (Pt. 1): College Station, TX (Ocean Drilling Program), 15–48.

Spezzaferri, S., and Premoli Silva, I., 1991. Oligocene planktonic foraminiferal biostratigraphy and paleoclimatic interpretation from Hole 538A, DSDP Leg 77, Gulf of Mexico. *Palaeogeogr., Palaeoclimatol., Palaeoecol.,* 83:217–263.

Suess, E., von Huene, R., et al., 1988. *Proc. ODP, Init. Repts.,* 112: College Station, TX (Ocean Drilling Program).

Thierstein, H.R., Geitzenauer, K.R., Molfino, B., and Shackleton, N.J., 1977. Global synchroneity of late Quaternary coccolith datum levels: validation by oxygen isotopes. *Geology,* 5:400–404.

von Herzen, R.P., and Maxwell, A.E., 1959. The measurement of thermal conductivity of deep-sea sediments by a needle probe method. *J. Geophys. Res.,* 64:1557–1563.

Wentworth, C.K., 1922. A scale of grade and class terms of clastic sediments. *J. Geol.,* 30:377–392.

Wilson, W.D., 1960. Speed of sound in seawater as a function of temperature, pressure and salinity. *J. Acoust. Soc. Am.,* 32:641–644.

Wyllie, M.R.J., Gregory, A.R., and Gardner, L.W. 1956. Elastic wave velocities in heterogeneous and porous media. *Geophysics,* 21:41–70.

Ms 154IR-102

APPENDIX A

Corrections to Reflectance Measurements

Reflectance measurements were taken on nearly all cores recovered under one of two scenarios: (1) covered with plastic wrap (brand Handi-Wrap), and (2) uncovered. Most cores that were covered are the uppermost cores of each hole. Appendix Table A-1 includes the total list of cores measured while covered with plastic wrap.

Plastic wrap affects the reflectance measurements as a function of both percentage of reflectance and wavelength. Empirical corrections were determined from linear regressions of "wrapped core" data onto "unwrapped core" data at each wavelength measured to account for the plastic-wrap bias. Appendix Table A-2 contains the information needed to correct these data if desired. All reflectance data available from ODP are uncorrected for the effect of plastic wrap.

Appendix Table A-1. Cores covered with plastic wrap.

Hole	
925B	Cores 1H–3H, 11H–18H
925C	Cores 1H–18H, 24H–38H
925D	Cores 1H–26H
925E	Cores 1H–end (6H)
926A	Cores 1H–20H
926B	Cores 1H–26H
926C	Cores 1H–20H
927A	Cores 1H–20H, 30H–end (33H)
927B	Cores 1H–end (28H)
927C	Cores 1H–26X
928A	Cores 1H–21H
928B	Cores 1H–19X
928C	Cores 1H–end (20X)
929A	Cores 1H–19X, 21X–22X
929B	Cores 1H–16X
929C	Cores 1H–end (16X)
929D	Cores 1H–end (6H)

APPENDIX A (continued).

Appendix Table A-2. Empirical correction factors to convert "wrapped core" reflectance measurements into "unwrapped core" data.

Wavelength (nm)	R^2	Intercept	Slope
400	0.8785	–2.6479	0.6882
410	0.9008	–3.1280	0.7214
420	0.9132	–3.2657	0.7422
430	0.9150	–3.0802	0.7520
440	0.9112	–2.7430	0.7549
450	0.9072	–2.4465	0.7562
460	0.9063	–2.2758	0.7594
470	0.9066	–2.1586	0.7627
480	0.9055	–1.9848	0.7643
490	0.9021	–1.7118	0.7639
500	0.8964	–1.3210	0.7618
510	0.8890	–0.8462	0.7579
520	0.8805	–0.3312	0.7532
530	0.8704	0.2715	0.7469
540	0.8574	0.9681	0.7367
550	0.8394	1.9377	0.7209
560	0.8154	3.1510	0.6986
570	0.7883	4.4398	0.6715
580	0.7655	5.5580	0.6467
590	0.7457	6.4555	0.6253
600	0.7334	6.9970	0.6108
610	0.7275	7.2008	0.6031
620	0.7225	7.3344	0.5982
630	0.7207	7.3479	0.5965
640	0.7187	7.3414	0.5951
650	0.7166	7.3275	0.5935
660	0.7162	7.2515	0.5935
670	0.7148	7.2258	0.5925
680	0.7136	7.1951	0.5914
690	0.7140	7.1039	0.5919
700	0.7141	7.0301	0.5911

Note: Correction equations are of the form: (corrected data) = slope × (uncorrected data) + intercept.

APPENDIX B

Corrections to Natural Gamma Data

The natural gamma counter was added to the MST track recently. Leg 154 scientists were led to its use by the availability of the preliminary report contributed by Leg 150 scientists. One recommendation of that group (Hoppie et al., in press) was that the five energy channels collected by the tool should be reset to match the five energy channels into which downhole natural gamma counts are binned. This would have two related advantages: (1) it would enable direct comparison with the downhole data, and (2) it would permit the same algorithms to be used for interpreting downhole and laboratory data in terms of rock type. Unfortunately, the instructions for setting the channels were not clearly written and were misinterpreted when the equipment was reset before the beginning of Leg 154; to facilitate subsequent correction, the resetting was done between Sites 925 and 926. Appendix Table B-1 gives the (incorrect) settings used for Site 925, and the (correct) settings used for Sites 926 to 929. It is not possible to reconstruct individual channel data for Site 925. An approximation to the correct total count may be obtained by summing the counts in channels 1, 2, and 3 in the Site 925 settings. We determined empirically that the correct figure is about 0.80 of this sum (corrected for background) by making 100-s counts at 10-cm intervals in Section 154-929D-4H-2 twice with correct and incorrect settings (equivalent to 140 comparisons at 10-s counts). For Site 925, the background count with a water-filled core liner was slightly different than the counts obtained for Sites 926–929: 9.88 cps vs. 7.92 cps, when the correct settings were used. We calculated background counts by running 107 water-filled liners and measuring counts over 10-s intervals. The collected statistics were used to correct each individual channel. These corrections are given in Appendix Table B-2. Natural gamma data on CD-ROM (back pocket) have been corrected using these values.

Appendix Table B-1. Range settings for natural gamma counters used during Leg 154.

Channel	Range set during Site 925 operations (KeV)	Correct range used for Sites 926–929 (KeV)
1	200.47–733.53	200–500
2	501.6–1624.4	500–1100
3	1102.3–2713.9	1100–1590
4	1591.1–3075	1590–2000
5	2001–3075	2000–3000

APPENDIX B (continued).

Appendix Table B-2. Background corrections to natural gamma data, Sites 926–929.

	Measurements (*N*)	Mean count number (cps)	SD (cps)
Total	107	7.918	1.091
Channel 1	107	4.599	0.860
Channel 2	107	2.112	0.527
Channel 3	107	0.663	0.263
Channel 4	107	0.198	0.143
Channel 5	107	0.346	0.168

Note: N = number of measurements taken, SD = standard deviation, and cps = counts per second.

APPENDIX C

Corrections to GRAPE Data

In the earlier part of Leg 154, we noticed that the counts recorded during a GRAPE calibration were often significantly different from those of the previous calibration, suggesting that a small element of drift had occurred in the equipment (standard policy is to run a calibration each 12-hr shift). By the end of the leg, it was still not clear what the cause of this problem had been; one likely candidate is a faulty power supply, but it was not possible to replace this item. Later in the leg, an apparently different (but conceivably related) problem was identified: the apparent GRAPE density rose by about 0.1 g/mL when the *P*-wave signal entered the core (or the water standard). Severe sensitivity to the emission of the vibra-pen used to mark core liners was also noticed. Fortunately, a large number of discrete bulk-density and porosity determinations were made at all Leg 154 sites; it is not yet clear to what extent the value of the GRAPE data can be enhanced retroactively. Meanwhile, readers are warned that the shipboard GRAPE data should be used with extreme caution. Regardless, these data are provided on CD-ROM (back pocket). Where multiple GRAPE measurements have been made at the same discrete depth, those values have been averaged.